

**THE REPUBLIC OF TURKEY
BAHÇEŞEHİR UNIVERSITY**

**KINEMATICS, DYNAMICS, AND INTEGRATION OF A
REDUNDANT MANIPULATOR FOR LAPAROSCOPIC
ROBOTIC SURGERY**

Master's Thesis

ALAA ALASSI

İSTANBUL, 2018

**THE REPUBLIC OF TURKEY
BAHÇEŞEHİR UNIVERSITY**

**THE GRADUATE SCHOOL OF NATURAL AND APPLIED SCIENCES
MECHATRONICS ENGINEERING**

**KINEMATICS, DYNAMICS, AND INTEGRATION OF
A REDUNDANT MANIPULATOR FOR
LAPAROSCOPIC ROBOTIC SURGERY**

Master's Thesis

ALAA ALASSI

Supervisor: Assist. Prof. Dr. BERKE GÜR

İSTANBUL, 2018

**THE REPUBLIC OF TURKEY
BAHÇEŞEHİR UNIVERSITY**

**The Graduate School of Natural and Applied Sciences
Mechatronics Engineering**

Title of the Master's Thesis : Kinematics, Dynamics, And Integration Of
a Redundant Manipulator for Laparoscopic
Robotic Surgery
Name/Last Name of the Student : Alaa ALASSİ
Date of Thesis Defense : 18 September, 2018

The thesis has been approved by The Graduate School of Natural and Applied Sciences.

Assist. Prof. Dr. Yücel Batu Salman
Graduate School Director
Signature

I certify that this thesis meets all the requirements as a thesis for the degree of Master of
Science.

Assist. Prof. Dr. Berke Gür
Program Coordinator
Signature

This is to certify that we have read this thesis and that we find it fully adequate in scope,
quality and content, as a thesis for the degree of Master of Science.

Examining Committee Members:

Signature

Thesis Supervisor
Assist. Prof. Dr. Berke Gür

.....

Member
Assist. Prof. Dr. Uğur Tümerdem

.....

Member
Assist. Prof. Dr. Tarkan Aydın

.....

ACKNOWLEDGEMENTS

I would like to thank my colleges; Abdul Rahman Dabbour, Rouein Fani, Mohammad Awad, Omar Albiek and Ahmet Ak for their support.

This work was supported by The Scientific and Technological Research Council of Turkey (TUBITAK) project 115E712.

İstanbul, 2018

Alaa ALASSI



ABSTRACT

KINEMATICS, DYNAMICS, AND INTEGRATION OF A REDUNDANT MANIPULATOR FOR LAPAROSCOPIC ROBOTIC SURGERY

Alaa Alassi

Mechatronics Engineering
Supervisor: Assist. Prof. Dr. Berke Gür

September 2018, 80 Page

The recent advancements in robotic manipulators have resulted in a successful utilization of these technologies in robotic-assisted surgeries, particularly minimally invasive surgeries (MIS). Robots not only augment the surgeon's capabilities in terms of precision and dexterity but also mitigate the physical and cognitive efforts of the surgeon during operations. Currently available commercial surgical systems (the da Vinci Surgical System, for instance) lacks the ability to reflect forces of tool-tissue interaction back to the surgeon's hand. Such inadequacy necessitates implementing bilateral teleoperation to introduce haptics to the system. To this end, a robotic platform design was proposed within the scope of a TUBITAK¹research project with the purpose of closing the gap in existing robotic surgical platforms by incorporating haptic force feedback to the system. The proposed design integrates the redundant 7-DoF manipulator Kuka IIWA with an in-house-designed 3+1-DoF wrist mechanism. The manipulator provides the pivoting motion that moves the wrist around the incision point. Whereas the wrist compensates the lost degrees of freedom due to the pivoting motion (Remote Center of motion **RCM**) Consequently, this produces results in two problems: firstly, such integration results in a complex inverse kinematic solution. Secondly, because the two systems use different controllers, it is necessary to develop a system architecture that integrates the manipulator and the wrist considering the real-time performance constraint. With this in mind, in this thesis, For the first problem, A geometric kinematic solution is obtained for the primary task that is to provide **RCM** for the combined manipulator-wrist structure so that surgeon motion is fully mapped to the forceps allowing intuitive manipulation. Utilizing the kinematic redundancy of IIWA a geometric kinematic solution is presented to perform a secondary task that optimizes the motion of IIWA while performing the primary task. For the Integration problem, A system architecture based on networking and multiprocessing is proposed to integrate the **RCM** manipulator, the wrist in addition to the haptic device. Moreover, dynamic analysis and a simulation environment of the manipulator is also provided. Finally, unilateral and bilateral experiments are performed to validate the actual

¹The Scientific And Technological Research Council of Turkey

system.

Keywords: Haptics, Remote Center Of Motion, Redundancy. System Architecture.



ÖZET

ARTIK SERBESTLİK DERECELİ LAPAROSKOPIK CERRAHİ ROBOTUNUN KİNEMATİĞİ, DİNAMİĞİ ve SİSTEM BÜTÜNLEŞTİRİLMESİ

Alaa Alassi

Mekatronik Mühendisliği
Tez Danışmanı: Dr. Öğr. Üyesi Berke Gür

Eylül 2018, 80 Sayfa

Son dönemde meydana gelen teknolojik gelişmeler, robot kollarının robot-destekli ameliyatlarda ve özellikle de minimal invazif cerrahide başarı ile kullanılmasını sağlamıştır. Robotlar yalnızca cerrahın kabiliyetlerini hassasiyet ve el-becerisi bakımından arttırmakla kalmayıp, aynı zamanda operasyon sırasında cerrahın üzerindeki fiziki ve bilişsel yükü de azaltmaktadır. Mevcut ticari robotik cerrahi sistemleri (örneğin, da Vinci robotik ameliyat sistemi) doku-alet arasındaki etkileşimden doğan kuvvetleri cerrahın eline yansıtma kabiliyetinden yoksundur. Bu eksikliği gidermek için gereken haptik yetenekler, robotik ameliyat sistemine çift-yönlü tele-operasyon yapısının uygulanması ile gerçekleştirilebilir. Bu amaç doğrultusunda ve TÜBİTAK projesi kapsamında bir robotik cerrahi platformu tasarlanmıştır. Tasarlanan bu robotik cerrahi sisteminin sahip olduğu haptik kuvvet geri besleme özelliği sayesinde mevcut ameliyat robotlarında yer alan bu boşluğun doldurulması hedeflenmiştir. Önerilen robotik cerrahi sistemi, artık 7 serbestlik derecesine sahip KUKA IIWA robot kolu ile proje ekibi tarafından tasarlanan, 3+1 serbestlik derecesine sahip özgün bir bilek mekanizmasından meydana gelmektedir. Robot kol, bilek mekanizmasının vücuda girdiği nokta çevresindeki dönel hareketini (uzak mesnet merkezi) sağlamaktadır. Buna karşılık, bilek mekanizması ise bu dönel hareket sonucu kaybedilen serbestlik derecelerini telafi eder. Bu yapı iki soruna yol açmaktadır. Öncelikle, robot kol ile bilek mekanizması birlikte, ters çözümü zor olan bir kinematik yapı oluşturmaktadır. Buna ek olarak, robot kol ve bilek mekanizmasının farklı kontrol yapılarına sahip olmaları sebebi ile, geliştirilen robotik cerrahi sisteminin gerçek zamanlı kontrolünü mümkün kılacak bir sistem ve yazılım mimarisi gereklidir. Bu tezde, yukarıda açıklanan bu iki soruna odaklanılmıştır. Ana görev olarak cerrahın tüm hareketlerinin tümleşik robot kol-bilek sistemi tarafından doğru bir şekilde tekrarlanması olarak belirlenmiştir. İlk sorunun çözümü için ana görevin gerçekleştirilmesini olanak sağlayacak geometrik bir kinematik ters çözüm geliştirilmiştir. KUKA IIWA robot kolunun artıklığından yararlanılarak, ana

görevin gerçekleştirildiği sırada, bu görevi etkilemeyecek şekilde ikincil bir görevin de gerçekleştirilmesini sağlayan geometrik bir kinematik çözüm de geliştirilmiştir. Uzak mesnet merkezi hareketini sağlayan robot kol, bilek mekanizması ve haptik özelliklere sahip bir kumanda kolunun bütünleştirilmesine olanak sağlayan, ağ yapısına ve çok işlemli mimariye sahip bir yapı önerilmiştir. Buna ek olarak, robot kolun dinamik analizi gerçekleştirilmiş ve bir benzetim ortamı geliştirilmiştir. Son olarak, önerilen çözümler ve sistemin başarımı tek-yönlü ve çift-yönlü deneyler ile doğrulanmıştır.

Anahtar Kelimeler: Haptik , uzak mesnet merkezi, kinematik artıklık, sistem mimarisi.



CONTENTS

TABLES	xi
FIGURES	xv
ABBREVIATIONS	xvi
SYMBOLS	xvii
1. INTRODUCTION	1
1.1 HISTORICAL TURNING POINTS TOWARD ROBOTIC SURGERY	3
1.2 A COMPARISON OF CONVENTIONAL AND ROBOTIC ASSISTED LAPAROSCOPIC SURGERY	5
1.3 THE ADOPTION OF RALS	6
1.4 IMPORTANCE OF HAPTIC FEEDBACK	7
1.5 GAP AND CONTRIBUTION	8
2. LITERATURE REVIEW	11
2.1 DA VINCI	11
2.2 S-SURG	12
2.3 RAVEN	13
2.4 MIRO	14
2.5 SENHANCE SURGICAL SYSTEM	15
3. KUKA IIWA KINEMATIC ANALYSIS	17
3.1 FORWARD KINEMATICS	17
3.2 TASK SPACE KINEMATICS	18
3.2.1 Joint one	19
3.2.2 Joint four	20
3.2.3 Joint two	21
3.2.4 Joint six	23
3.2.5 Joints five and seven	24
3.3 POSTURE KINEMATICS	25
3.3.1 7-DOFS INVERSE KINEMATICS SOLUTION	26
3.4 REDUNDANCY RESOLUTION	30
3.4.1 Score Function	30
3.4.2 Experimental Analysis	34

3.4.3	Iterative Optimization Algorithm	38
3.4.4	Iterative Optimization Algorithm Experiments	39
3.4.5	Hill Climbing Algorithm	43
4.	KUKA IIWA DYNAMIC ANALYSIS	45
4.1	INTRODUCTION	45
4.2	DYNAMIC MODELING	46
4.3	THE PROPOSED ALGORITHM	48
4.4	EXPERIMENTS AND VALIDATION	49
4.4.1	Validation by Simulation	50
4.4.2	Validation by Force/Torque Sensor	52
5.	TROCAR KINEMATICS	55
5.1	VIRTUAL LAPAROSCOPIC ROBOTIC INSTRUMENT	56
5.2	FORWARD KINEMATICS	58
5.3	INVERSE KINEMATICS	59
5.4	JACOBIAN AND SINGULARITY ANALYSIS.....	62
5.5	POSITION CONTROL	63
6.	SIMULATION.....	65
6.1	INTRODUCTION	65
6.2	MATLAB-SIMULINK SIMULATION ENVIRONMENT.....	65
7.	SYSTEM ARCHITECTURE AND IMPLEMENTATION	68
7.1	SYSTEM COMPONENTS	68
7.1.1	Omega.6	68
7.1.2	The Kuka IIWA 7 R800 Robot.....	68
7.1.3	The Wrist Mechanism	68
7.2	SYSTEM INTEGRATION	69
7.3	DATA FLOW AND SIGNAL TRANSFER	71
8.	EXPERIMENTS and RESULTS	73
8.1	VALIDATION OF ROTATIONAL MOTION	73
8.2	BILATERAL TELEOPERATION EXPERIMENTS	75
9.	CONCLUSIONS	79
	REFERENCES	81
	APPENDICES.....	86

Appendix A. 1	Senhance system and Da-Vinci comparison table	87
Appendix A. 2	TUBITAK Project Work packages	88



TABLES

Table 3.1 :	KUKA LBR IIWA Denavit-Hartenberg parameters based on the modified convention	17
Table 3.2 :	Algorithm validation. Angles are measured in Degree	39
Table 3.3 :	Comparison of joint angles before and after the optimization.....	40
Table 4.1 :	Mean squared error of joint torques.....	51
Table 5.1 :	DH parameters of the Virtual Laparoscopic Robotic Instrument ...	58
Table 8.1 :	Statistical values of the rotational motion experiment. The values are measured in millimeters.	73



FIGURES

Figure 1.1 : Minimally invasive surgery	2
Figure 1.2 : Types of the endoscope	2
Figure 1.3 : PUMA 200 holding a probe in brain biopsy procedure	4
Figure 1.4 : significant events that shaped modern MIS.	5
Figure 1.5 : Cases of robotic surgeries.	7
Figure 1.6 : The slave side of the surgical robotic platform. (a)KUKA IIWA 7-DoF Manipulator. (b) The combined 10+1-DoF system .(c) The 3+1-DoF robotic wrist developed by (Bazman et al., 2018).	9
Figure 1.7 : Omega.6; the master side of the surgical robotic platform.	9
Figure 2.1 : The da Vinci System.(a)Surgeon Console, (b) Patient-Side Cart, (c) The RCM mechanism arm serially coupled with the EndoWrist and (d) the Vision System.	12
Figure 2.2 : (a) S-surge surgical robot. (b) S-surge Master-Slave System.	13
Figure 2.3 : (a) Raven. (b) RavenII.	14
Figure 2.4 : MIRO surgical robotic system.	15
Figure 2.5 : Senhance Surgical System architecture.	16
Figure 3.1 : Frame assignment for KUKA LBR IIWA.	17
Figure 3.2 : Geometric analysis regarding Joint angle θ_1	19
Figure 3.3 : Elbow left configuration.	22
Figure 3.4 : Elbow right configuratione θ_1	23
Figure 3.5 : Geometrical analysis regarding joint angle six.	24
Figure 3.6 : The geometry of posture motion.	25
Figure 3.7 : An example configuration to illustrate Joints 1 and 3 flipping problem. (a) Non-reversed coordinates, $\theta_1 = 122$ and $\theta_3 = 160$ Degree. (b) Reversed coordinates, $\theta_1 = 58$ and $\theta_3 = -20$ Degree .	27
Figure 3.8 : The geometrical analysis of joint angles one and seven.	29
Figure 3.9 : The polar plot of the cost as it varies with the arm angle δ . The star represents the global minimum at which δ is optimal.	31
Figure 3.10 : The polar plot of the exponential scores for each value of arm angle δ . The star represents the global maximum at which δ is optimal.	32

Figure 3.11 : The polar plot of the exponential scores for each value of arm angle δ . The star represents the global maximum at which δ is optimal.	34
Figure 3.12 : Tuning the score function(a) $\lambda = 10$. (b) $\lambda = 100$	34
Figure 3.13 : Optimization of configuration A by rotating the arm angle.(a) initial configuration .(b) optimized configuration.(c) Score function with the optimal arm angle represented by the red circle.	36
Figure 3.14 : Optimization of configuration A' by rotating the arm angle.(a) initial configuration .(b) optimized configuration.(c) Score function with the optimal arm angle represented by the red circle.	36
Figure 3.15 : Optimization of configuration B by rotating the arm angle.(a) initial configuration .(b) optimized configuration.(c) Score function with the optimal arm angle represented by the red circle.	37
Figure 3.16 : Optimization of configuration B' by rotating the arm angle.(a) initial configuration .(b) optimized configuration.(c) Score function with the optimal arm angle represented by the red circle.	37
Figure 3.17 : The algorithm convergence for configuration A'.	40
Figure 3.18 : The algorithm convergence for configuration B'.	41
Figure 3.19 : Real-time joint limit avoidance. The blue line represents the 6-DoF joint trajectory. While the dashed red line represents the 7-DoF joint trajectory. The upper and lower limit of each joint is represented by the dotted lines. The x axis is the time in milliseconds.	42
Figure 3.20 : Real-time joint limit avoidance using the Hill Climbing Algorithm . The blue line represents the 6-DoF joint trajectory. While the dashed red line represents the 7-DoF joint trajectory. The upper and lower limit of each joint is represented by the dotted lines. The x axis is the time in milliseconds.	44
Figure 4.1 : Joint space trajectory. The joints are actuated successively from first to seventh joint.	51
Figure 4.2 : Model and actual torques using Sturs vales.	52
Figure 4.3 : Model and actual torques using Cad vales.	52
Figure 4.4 : Experiment setup.	53
Figure 4.5 : calculated End-effector Forces and torques validated with Force/torque sensor measurements.	54
Figure 5.1 : RRPR Model of the manual laparoscopic motion.	57
Figure 5.2 : Frame assignment of the Virtual Laparoscopic Robotic Instrument using the modified convention.	58

Figure 5.3 :	Visualization of the RCM joints ϕ, ψ and ρ in addition to \vec{P}_G and \vec{d} vectors.	60
Figure 5.4 :	The control block diagram of the combined Wrist-Manipulator structure. Blocks that are red framed with a dashed line represents work conducted by (Bazman et al., 2018). Blocks that are orange framed with a dotted line represents joint work documented in (Alassi et al., 2018). Blocks framed otherwise are thesis work.	64
Figure 6.1 :	Omega.6 interface to Simulink implemented using inlined C++ S-Function.	66
Figure 6.2 :	The Contact force with their corresponding to virtual walls. Forces are generated whenever the position is less than zero along the three dimensions.	66
Figure 6.3 :	Pitch, Yaw and Roll control through the integrated haptic device. The commanded values are: a) and b) yaw near 90 and -90 respectively, c) and d) Pitch near 45 and -70 respectively and e) is the initial orientation where roll, pitch, and yaw are zeros.	67
Figure 7.1 :	A functional diagram representing the distributed control scheme of the proposed surgical robotic platform. Blocks that are red framed with a dashed line represents work conducted by (Bazman et al., 2018) and (Yilmaz et al., 2018). Blocks that are orange framed with a dotted line represents joint work documented in (Alassi et al., 2018). Blocks framed otherwise are thesis work	70
Figure 7.2 :	A flow chart representing the communication logic.	71
Figure 7.3 :	Signal Packing.	72
Figure 8.1 :	(a) Posture plot of the Virtual Laparoscopic Robotic Instrument for randomly showing the gripper (magenta) and its frame while approaching a target point from different directions. The insertion link (black) performing RCM motion .Where (a) is a 3D perspective and (b) depicts the view from X-Y axis	74
Figure 8.2 :	Rotational Experiment Data.	74
Figure 8.3 :	The Random translational motion of the gripper.	75
Figure 8.4 :	Bilateral teleoperation experiments.	76
Figure 8.5 :	Experiment results for x-axis. (a) Shows the position of the TCP and the object's edge, a contact occurs each time the TCP crosses object edge towards the negative x. (b) Depicts the reaction force that is reflected to the master side.	77

Figure 8.6 : Experiment results for y-axis. (a) Shows the position of the TCP and the object's edge, a contact occurs each time the TCP crosses object position towards the negative y. (b) Depicts the reaction force that is reflected to the master side. 77

Figure 8.7 : Experiment results for z-axis. (a) Shows the Euler angle γ . (b) Depicts the robot torque that is induced by the robot according to Hooke's law 78

Figure A.1 : Senhance system and Da-Vinci comparison table 87



ABBREVIATIONS

CLS	:	conventional laparoscopic surgery
MIS	:	Minimally Invasive Surgery
MIRS	:	Minimally Invasive Robotic Surgery
RALS	:	Robot-assisted laparoscopic surgery



SYMBOLS

Centripetal force matrix	:	\mathbf{c}
Cost function	:	C
Force	:	\mathbf{f}
Gravity vector	:	\mathbf{g}
Generalized inertia matrix	:	\mathcal{M}
Homogeneous transformation matrix	:	\mathbf{T}
Inertia matrix	:	\mathbf{M}
Jacobian matrix	:	\mathbf{J}
Manipulator torque vector	:	$\mathbf{\Gamma}$
Moment	:	n
Score function	:	S
Score function tuning factor	:	λ

1. INTRODUCTION

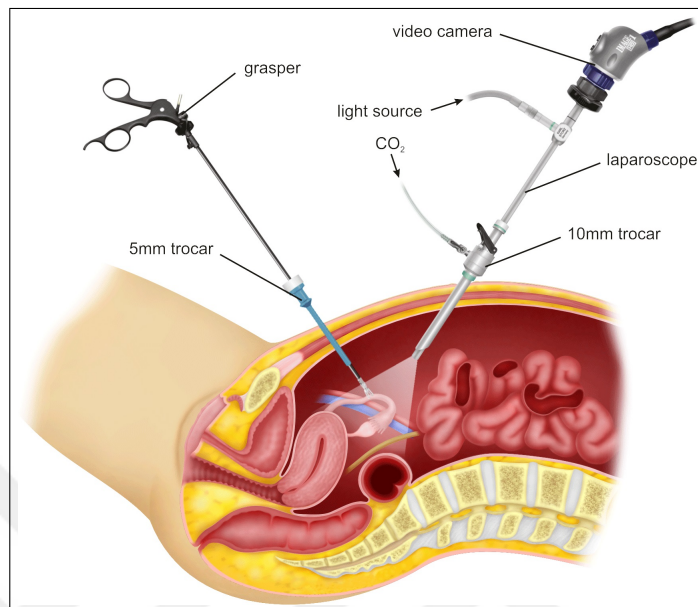
In open surgeries, a large incision is necessary for two reasons

- (a) To expose the operative field to surgeon sight.
- (b) To provide adequate workspace for the tools together with the surgeon's hands so that he can approach the target and accomplish the desired motion.

The implications of such an incision are; blood losses during the operation, post surgery trauma, long recovery time in addition to cosmetic issues. These drawbacks of open surgeries motivated surgeons to come up with a better technique termed "Minimally Invasive Surgery" (MIS) also known as Laparoscopic surgery (Lee-Kong & Feingold, 2013). In this approach, a small incision is made to accommodate enough entry area for only the surgical tools as depicted in figure 1.1. Mechanically, the method utilizes a basic motion transition technique known as the Remote center of motion (RCM)(Aksungur, 2015) whereby tools are remotely manipulated. However, MIS method implies that the internal organs are not exposed to the surgeon's field of vision, as a result, the development of MIS was dependent on the evolution of the endoscope which is an optical device used to provide a subcutaneous view of the operative field (Figure 1.2). The drawbacks of RCM in addition to the need for stable and tremor-free endoscopic view encouraged engineers to incorporate robots into MIS procedures.

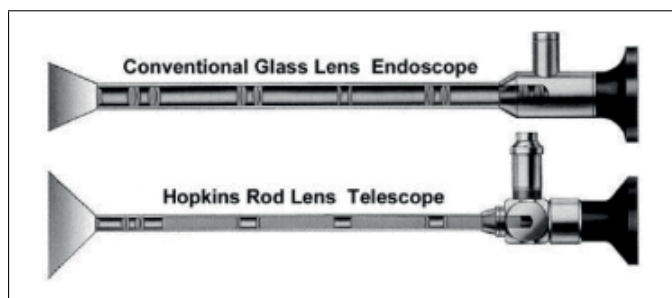
In this chapter, we first illustrate the historical milestones that shaped modern MIS and the events that led to what is known today as Minimally Invasive Robotic Surgery(MIRS) also referred to as Robot-assisted Laparoscopic Surgery RALS. After that comes a comparison between RALS and CLS (Conventional Laparoscopic Surgery) followed by a statistical study on the adoption of RALS. Then we present a study that emphasizes the importance of haptics in MIS and we finish the chapter by stating the gap and the contribution of this thesis.

Figure 1.1: Minimally invasive surgery



Source: <http://www.continentalhospitals.com/blog/>

Figure 1.2: Types of the endoscope



Source: De Groen (2017)

1.1 HISTORICAL TURNING POINTS TOWARD ROBOTIC SURGERY

Historically Gorge Kelling was the first physician who conducted laparoscopy on a dog back in 1901, and after a decade, Hans Christian Jacobaeus published the first paper regarding the possibilities and limitation of laparoscopy that he performed on a human patient (De Groen, 2017). To this point, MIS seemed to be a promising technique as it introduced several advantages over the conventional open surgeries such as; mitigating pain and blood losses, faster recovery, fewer Scars, less hospital stay in addition to reducing the possibility of infection. Nonetheless, the procedure was not easily performed due to lack of a high-quality endoscope (De Groen, 2017).

In the the year 1959, surgery witnessed an unprecedented evolution after the surgeon-scientist Harold Hopkins engineered the rod-lens endoscope (figure1.2) (Vitiello et al., 2013)(De Groen, 2017). Hopkins endoscope solved the problems of the conventional glass endoscope by providing a wider range, sharper colored image, and satisfactory lighting conditions, thanks to fiber optics bundle that was utilized to transfer the light. This was the starting point of the modern laparoscopy (De Groen, 2017).

This improvement has shifted the problem from patients to doctors as from now they have to deal with challenges such as:

- (a) cognitive effort on the surgeon due to handling the mapping required to mirror and scale the motion of the laparoscopic tool inside the patient, this problem is known as the fulcrum effect (Gallagher et al., 1998).
- (b) physical effort introduced by the friction between the tool and the canal (trocar) through which the tool is passing.
- (c) reduced dexterity
- (d) degradation of tactile feedback.
- (e) Tremor magnification.

Figure 1.3: PUMA 200 holding a probe in brain biopsy procedure



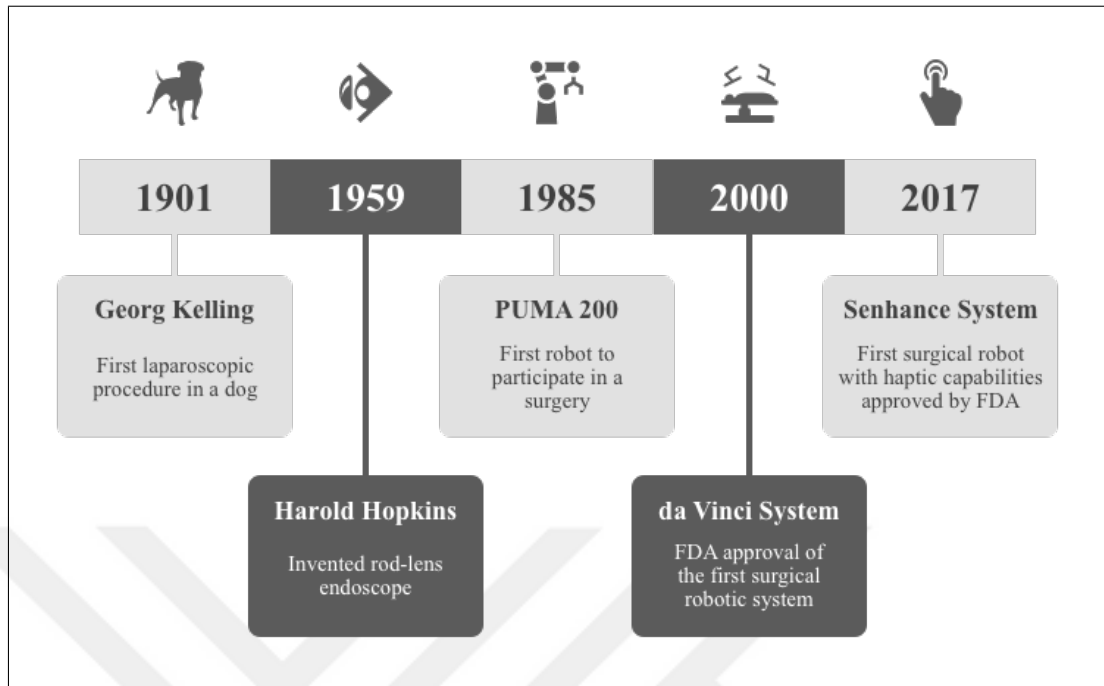
Source: gelookahead.economist.com

These cons have formed the entry point for the robotic manipulator to the MIS field. this caused the problem to get shifted once again but this time to engineers. Several attempts were carried out Since the mid 80's to engage robots in surgery, The participation of the industrial robot PUMA 200 (figure 1.3) in a brain biopsy despite the fact that it was restricted to probe placement (Kwoh et al., 1988) was the starting point for robotic-assisted surgeries. After that, bolder steps have been achieved toward deeper involvement in surgery tasks.

An important milestone in robotic MIS was reached in the year 2000 when the da Vinci Surgical System by Intuitive surgical received the FDA approval (Kalan et al., 2010). Since then, Da Vinci has become the primary robotic system for general purpose laparoscopic surgery (Rao, 2018). Da Vinci introduced substantial improvements to MIS. Among these improvements are higher accuracy, precision, motion scaling, elimination of fulcrum effect, enhanced dexterity as well as tremor filtering (Mack, 2001).

However, da Vinci was lacking a crucial element of an effective RALS procedure which is haptics, that is, the ability to reflect the forces of tool-tissue interaction back to the surgeon's hand. Only recently, two haptically enhanced surgical robots became available to the market, namely the Senhance System and REVO (Rao, 2018). The former is a

Figure 1.4: significant events that shaped modern MIS.



commercial version of ALF-X (Gidaro et al., 2012) approved by the FDA. The ALF-X was also granted the CE mark for the European market. The latter system is approved by the Korean FDA only (Rao, 2018) and, therefore is currently restricted to the Korean market. The arrival of these two systems opens a new chapter in the ongoing development of surgery and indicates that haptics is its title. Figure 1.4 depicts the evolutionary steps of MIS.

1.2 A COMPARISON OF CONVENTIONAL AND ROBOTIC ASSISTED LAPAROSCOPIC SURGERY

Memon et al. (2012) compared between robotic-assisted laparoscopic surgery (RALS) and Conventional Laparoscopic Surgery (CLS) from the patient perspective, they concluded that there were no remarkable differences in terms of complication, or hospital stay, however, procedures performed with robots showed less tendency to convert to open surgery than conventional laparoscopy.

On the other hand, instead of focusing on the patient, Nguan et al. (2008) compared the performance of physicians when operating using CLS, ZEUS, and da Vinci system. The study showed the superiority of the da-Vinci system over the CLS and ZEUS, moreover, it showed that CLS outperforms ZEUS system. This inferiority of ZEUS system is due to the lack of important features such as;

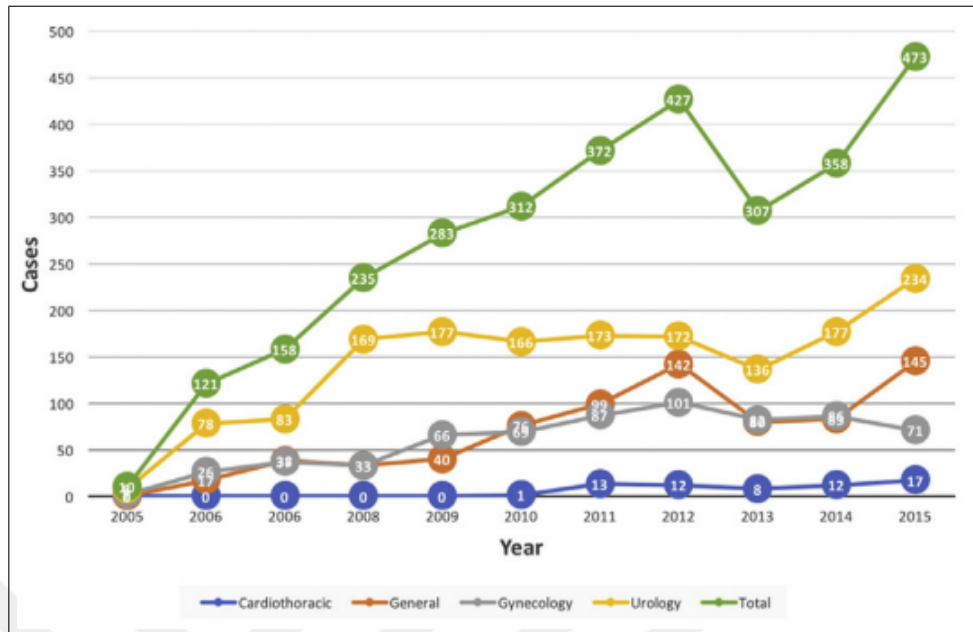
- (a) 2-DoF endowrist.
- (b) Tactile feed back.
- (c) Poor 2D visualization.

The study concluded that experienced staff can adapt rapidly to da vinci system and exploit it in more sophisticated procedures.

1.3 THE ADOPTION OF RALS

A study performed at the University of California San Diego medical center by Stringfield et al. (2017) evaluated 3,203 robotic surgery operation conducted over 10 years. The study concluded that robotic surgeries quadrupled along these 10 years. Furthermore the study reported that between the year 2015 and 2016 length of stay for a patient who had robotic surgery was 1.8 days shorter than their counterparts with an open surgery procedure, However, the overall cost almost doubled. the study also showed A remarkable increase in the adoption of robotic-assisted surgeries among urologists as compared to a slight increase among cardiologist as illustrated in figure 1.5.

Figure 1.5: Cases of robotic surgeries.



Source: Stringfield et al. (2017)

1.4 IMPORTANCE OF HAPTIC FEEDBACK

Wagner et al. (2007) hypothesized that the availability of haptic feedback in RALS is vital for the effective performance of surgeries. To prove this point, they designed a controlled experiment to determine the benefits of having force feedback reported to the surgeon during surgery. The study concluded that force feedback contributes to the overall quality of surgery with three main factors:

- Force feedback in real-time renders the mechanical properties of the tissue at a master command interface, providing virtual constraints on the surgeon's motion, such constraint results in a more precise tissue dissection.
- higher fidelity in force feedback results in faster dissection.
- reduction in cognitive efforts spent by surgeons to extract haptic perception from

visual information.

1.5 GAP AND CONTRIBUTION

Despite the advent of haptically enhanced robotic systems represented by Senhance System and REVO, technical details about the kinematic design, system architecture, and haptic rendering degrees-of-freedom (DOF) are not published for either system. Hence, the design of robotic platforms with haptic capabilities for MIS remains a matter of active research and development. In addition, the increment of the adoption of RALS and the absence of haptic in the most used RALS system in the world (da Vinci), calls out the need to develop a surgical robot with haptic feedback capabilities. Toward this end, in this thesis, research conducted as a part of the TUBITAK funded project¹ entitled "Designing and developing a minimally invasive surgical forceps with force feedback capabilities" is presented.

The objective of the project is to introduce a new robotic MIS system design that addresses the shortcomings of existing robotic MIS systems. The proposed surgical robotic platform provides:

- (a) 6-DOF surgical tool motion,
- (b) 6-axis force/torque feedback,
- (c) back-drivability,
- (d) modularity.

The proposed architecture integrates the compliant commercial 7-DOF *KUKA LBR IIWA 7 R 800* manipulator with an in-house designed 3-DOF parallel wrist mechanism as depicted in figure 1.6. This combined system is teleoperated using a 6-DoF haptic device

¹Refer to Appendix A. 2. for more details.

Figure 1.6: The slave side of the surgical robotic platform. (a) KUKA IIWA 7-DoF Manipulator. (b) The combined 10+1-DoF system. (c) The 3+1-DoF robotic wrist developed by (Bazman et al., 2018).

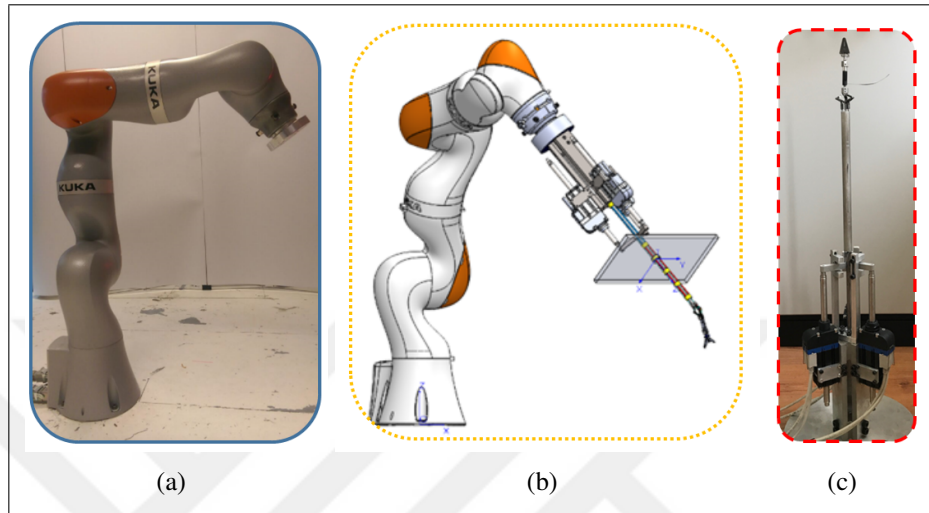


Figure 1.7: Omega.6; the master side of the surgical robotic platform.



Omega.6 which represents the master side (figure 1.7). Since this integration results in a hyper-redundant system with complex kinematics, the objective of this thesis is to introduce a kinematic analysis method termed the 'Virtual Laparoscopic Robotic Instrument' through which the surgical instrument motion is decoupled from the kinematics of the driving mechanism. This decoupling simplifies the inverse kinematics and singular configuration solutions of the surgical tool without dealing with the complexities of the driving manipulator. Also to perform kinematic and dynamic analysis of the driving manipulator IIWA robot supported by simulation and experimentally validated results. In addition to performing Human-in-the-loop simulation to enable the user to test the system in the virtual environment before using the real system. Finally, an architecture is proposed to integrate the major components of the platform whereby bilateral teleoperation is performable. To summarize, the contribution of this work is:

- (a) The concept of a Virtual Laparoscopic Robotic Instrument (VLRI) is proposed for solving the trocar kinematics.
- (b) The kinematic and dynamic analysis the KUKA IIWA robot was performed along with experimental validation.
- (c) Implementing Human-in-the-loop (HITL) simulation by integrating the used haptic device to the simulation environment.
- (d) Proposing and implementing integration architecture to perform bilateral teleoperation on the platform.

Due to the cooperative nature of this project, items (a) and (d) includes block diagrams that contain work performed by (Bazman et al., 2018) and (Yilmaz et al., 2018), these blocks are red framed with a dashed line. Also contains joint work documented in (Alassi et al., 2018) these blocks are orange framed with a dotted line. Blocks framed Otherwise are thesis work.

2. LITERATURE REVIEW

From a kinematic point of view (excluding soft robots) surgical robots can be classified into two major categories based on the approach through which RCM is accomplished:

- (a) Hardware based remote center of motion
- (b) Software based remote center of motion

In the first one, the pivoting motion around the incision is maintained through a mechanism with two intersecting joint axes at the RCM. which is the case in various surgical systems such as: da-Vinci, RAVEN and S-surg. Whereas, in the second category, the instrument is manipulated by a serial robot whereby the RCM motion is accomplished through the robot controller (Position, force or velocity control) (Aghakhani et al., 2013). this approach is used in MIRO and Versus. The main advantage of the software based RCM approach is the ability to change the RCM location by resetting its value in the program. with this in mind, in this chapter, we survey the current commercial and the state of the art surgical robotic platforms with emphasis on three main aspects (if available in the literature):

- (a) The mechanical design to achieve RCOM motion.
- (b) The methodologies of acquiring the force of contact with the tissue (if provided by the platform).
- (c) The system architecture.

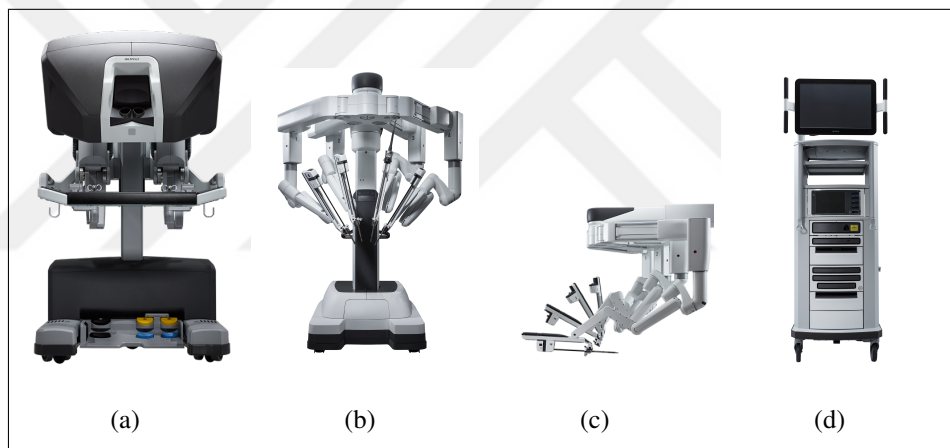
2.1 DA VINCI

da-Vinci is the most used surgical platform around the globe. According to Brisson (2017) the system consists of a "Surgeon Console" containing the master 6-DoF manipulators

and foot switches in addition to a 3D monitor dedicated only to the surgeon. And a Patient-Side Cart which is the part that includes four robotic arms each of which is a double parallelogram mechanism that performs hardware-based RCM motion while holding a 4-DoF robotic instrument termed "EndoWrist". Hence the system can accomplish 6-Dof Cartesian motion of the instrument.

The system is also equipped with a "Vision System" which provide a 3D HD visualizing on a monitor visible to the surgical crew. However, the system lacks haptic force feedback, instead, the magnitude of the force is projected on the monitor to give a clue about forces exerted on the tissue. Figure 2.1 illustrates the da-Vinci system.

Figure 2.1: The da Vinci System.(a)Surgeon Console, (b) Patient-Side Cart, (c) The RCM mechanism arm serially coupled with the EndoWrist and (d) the Vision System.



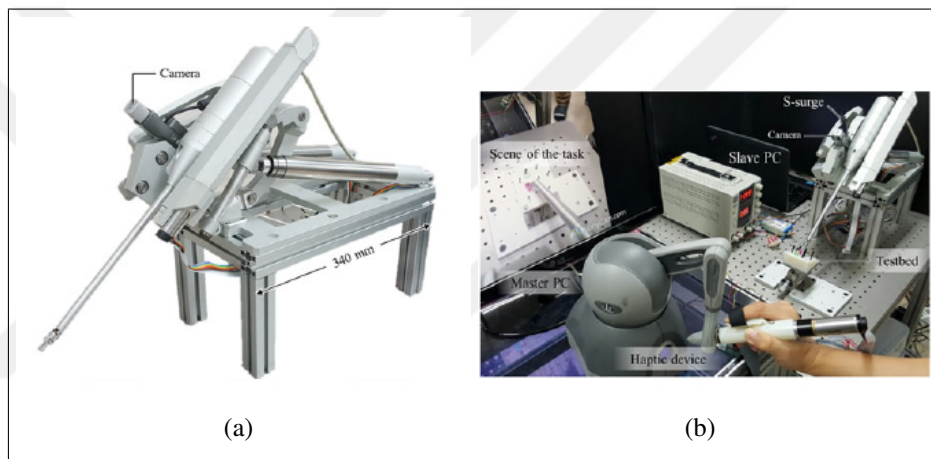
Source: ©2018 Intuitive Surgical, Inc.

2.2 S-SURG

Kim et al. (2017) discussed the pros and cons of three types of RCM mechanisms, spherical serial mechanisms SS, spherical parallel SP mechanisms and the double parallelogram mechanisms DP. Based on their discussion, they developed "S-surge" a hybrid mechanism combining SP and DP mechanisms by taking the advantage of the large workspace of DP,

and the improved accuracy of SP mechanisms. S-Surge is comprised of a 3-DOF hybrid remote center of motion (RCM) mechanism integrated with a 4-DOF surgical instrument. The master controller is the 3-DoFs phantom Omni haptic device, and the communication between the components of the system is ROS (Robot Operating System) based. Although S-Surge supports 6-DOF motion with one additional grasping DOF. The kinematic analysis provided for the system does not include the combined manipulator/instrument system and is limited to the 3-DOF RCM mechanism. Furthermore, feedback is limited to the 3 manipulating and one grasping DoF. Figure 2.2 depicts the S-surge platform.

Figure 2.2: (a) S-surge surgical robot. (b) S-surge Master-Slave System.



Source: Kim et al. (2017)

2.3 RAVEN

Lum et al. (2009) developed RAVEN system (Figure 2.3) which is a surgical robotic platform that provides 6 motion DOF and an additional grasping DOF. The design of RAVEN was kinematically optimized based on a database of spatial and dynamic measurements. Later on, The robot was enhanced with a ROS based software environment with the purpose of accelerating the implementation of artificial Intelligence related functions (machine learning, robot vision, and motion planning), the platform named "RavenII" was

adopted by many pioneering universities and as a result, an active network to share knowledge and data regarding the research conducted on the platform was established (Hannaford et al., 2013). However, RAVEN is also a mainly cable driven mechanism which introduces back-drivability issues manifested in the controller, as well as contact force estimation problems due to the nonlinear characteristic of the cables (Kosari et al., 2013).

Figure 2.3: (a) Raven. (b) RavenII.



Source: (a) Lum et al. (2009), (b) Hannaford et al. (2013).

2.4 MIRO

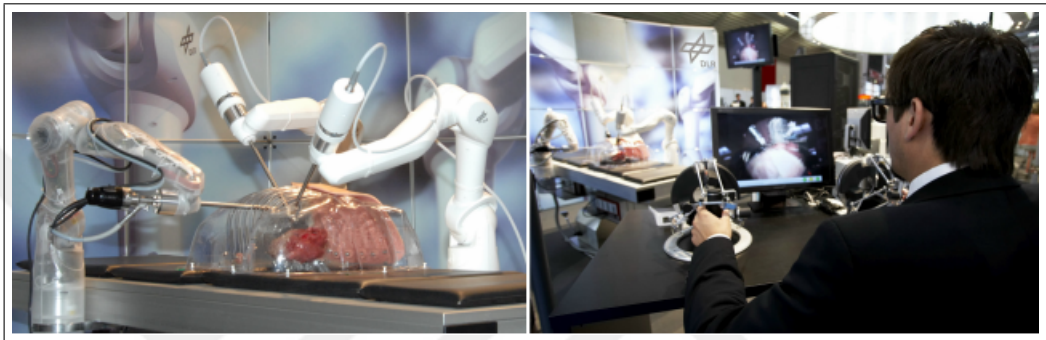
MIRO (Figure 2.4) is a surgical robotic platform developed by the German Aerospace Center (DLR) (Schlenk et al., 2018)(Konietschke et al., 2009) (Hagn et al., 2008a), the robot was designed with the purpose of providing versatility, modularity and compactness. Unlike S-surge and Raven, the kinematics of MIRO platform allows a wider spectrum of MIRS producers. MIRO fundamental advantages over existing commercial system are the flexibility it possesses by having a custom number of robotic arms performing the surgery, unlike the all-in-one approach that is applied in da Vinci. This separation of operating units has two advantages

1- the possibility to place the arm such that a staff member can participate in the procedure with more comfort.

2- economically it is more efficient as one can choose the necessary amount of arms for a specific surgery. For example, if the task is to perform a laparoscopy to inspect a tumor, then, for such a task, using one arm holding an endoscope is adequate.

MIRO is also equipped with a miniaturized 6 Axis force torque sensor that is able to measure 6 axis forces and torques of tool-tissue interaction. This increases the costs of laparoscopic tools as each of them must be equipped with such a sensor.

Figure 2.4: MIRO surgical robotic system.



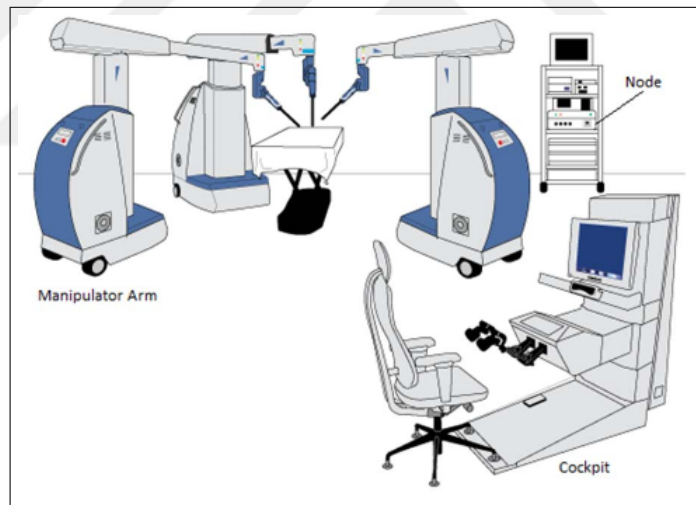
Source: Konietschke et al. (2009)

2.5 SENHANCE SURGICAL SYSTEM

As mentioned earlier in the introduction, the Senhance Surgical System is the first FDA approved robotic surgical platform that supports haptic feedback. Due to the scarcity of academic publication regarding the engineering aspect of the platform (kinematics, dynamics, system architecture), the review provided here is derived from the clearance report issued lately by the FDA for the manufacturer TransEnterix™ (Food and Drug Administration, 2017). Senhance System is originally developed from TELELAP ALF-X (Gidaro et al., 2012) surgical platform. The master-slave architecture of this platform (Figure 2.5) resembles the one da Vinci system has, A master console provides 2d/3d video monitor, in addition to two haptic handles for bilateral manipulation. A node unit to manage signal routing between the master and the slave. and finally, the robotic arms that

perform the RCM motion. The Superiority of Senhance platform to da Vinci is manifested in the availability of haptic force feedback in addition to Surgeon's gaze tracking feature which was integrated for safety reasons (Stopping the system if gaze is lost). However, Senhance System is inferior to its counterpart in the approach through which the instrument is manipulated. Sysnhace System is limited to the traditional 4-Dof laparoscopic motion, therefore the problem of RCM motion persists (mirrored motion). This puts the necessity of such systems in question. The reason behind retaining the conventional approach in Synhance System is perhaps to target the physician who already developed the CLS skills and it might not be effective for them to cope with the 6-DoF Cartesian motion approach. Aside from motion, force measurement is implemented by placing a 3 axis force sensor at the flange of the arm that is holding the instruments hence the system lacks the ability to measure the applied torques (Gidaro et al., 2012).

Figure 2.5: Senhance Surgical System architecture.



Source: (Food and Drug Administration, 2017).

3. KUKA IIWA KINEMATIC ANALYSIS

3.1 FORWARD KINEMATICS

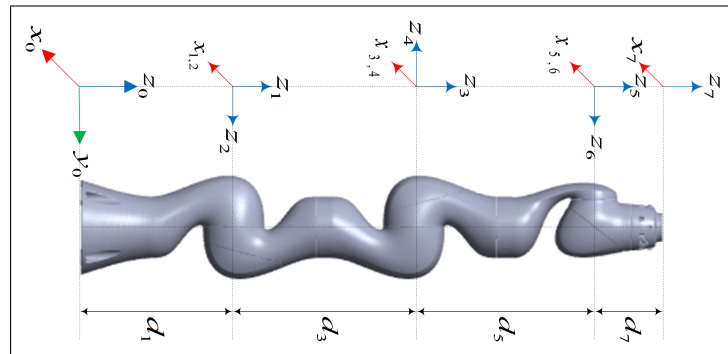
obtaining the forward kinematic matrices is a significant step for both dynamic and inverse kinematics. The kinematic model of the KUKA LBR IIWA is developed based the modified convention (Craig, 2005, pp.62-100). The zeroth frame is assigned to the base of the robot. Thus, the end effector z -coordinate gives the elevation of the robot end-effector from the ground. Table 3.1 contains the Denavit-Hartenberg (DH) parameters based on the frame assignments illustrated in Figure 3.1.

Table 3.1: KUKA LBR IIWA Denavit-Hartenberg parameters based on the modified convention

i	α_{i-1}	a_{i-1}	d_i	θ_i
1	0	0	d_1	θ_1
2	$-\pi/2$	0	0	θ_2
3	$\pi/2$	0	d_3	θ_3
4	$\pi/2$	0	0	θ_4
5	$-\pi/2$	0	d_5	θ_5
6	$-\pi/2$	0	0	θ_6
7	$\pi/2$	0	d_7	θ_7

The homogeneous transformation of each link with respect to the base is calculated Re-

Figure 3.1: Frame assignment for KUKA LBR IIWA.



cursively through:

$${}^0\mathbf{T} = {}^0_{i-1}\mathbf{T} \cdot ({}^{i-1}\mathbf{T}) \quad (3.1)$$

where the homogeneous transform ${}^{i-1}\mathbf{T}$ is computed as

$${}^{i-1}\mathbf{T} = \begin{bmatrix} \mathbf{c}\theta_i & -\mathbf{s}\theta_i & 0 & a_{i-1} \\ \mathbf{s}\theta_i\mathbf{c}\alpha_{i-1} & \mathbf{c}\theta_i\mathbf{c}\alpha_{i-1} & -\mathbf{s}\alpha_{i-1} & -\mathbf{s}\alpha_{i-1}d_i \\ \mathbf{s}\theta_i\mathbf{s}\alpha_{i-1} & \mathbf{c}\theta_i\mathbf{s}\alpha_{i-1} & \mathbf{c}\alpha_{i-1} & \mathbf{c}\alpha_{i-1}d_i \\ 0 & 0 & 0 & 1 \end{bmatrix} \quad (3.2)$$

with $\mathbf{c}\theta$ and $\mathbf{s}\theta$ indicating the cosine and sine of θ , respectively. The lines labelled as "Forward Kinematics" in the pseudo code 1 encapsulates equations (3.1) and (5.1).

3.2 TASK SPACE KINEMATICS

Inverse kinematics is the process of obtaining the joint angles given the desired position and orientation of the end effector. Consequently in this problem, the transformation matrix of the end effector 0_7T is always a known variable and can be utilized to obtain the joint angles.

The derivation of the inverse kinematics of IIWA is based on the geometric approach that is performed by (Khatamian, 2015) on the six degrees of freedom industrial manipulator KUKA KR60. Although the proposed approach provides an analytic inverse kinematic solution, it doesn't discuss the choices of joint angles in case of a non-unique solution.

To avoid the redundancy problem, the solution assumes that the third joint of IIWA is locked (always set to zero),

Note. 1: Any Vector with this form $i\vec{O}$ represents the position vector of frame $\{i\}$ w.r.t

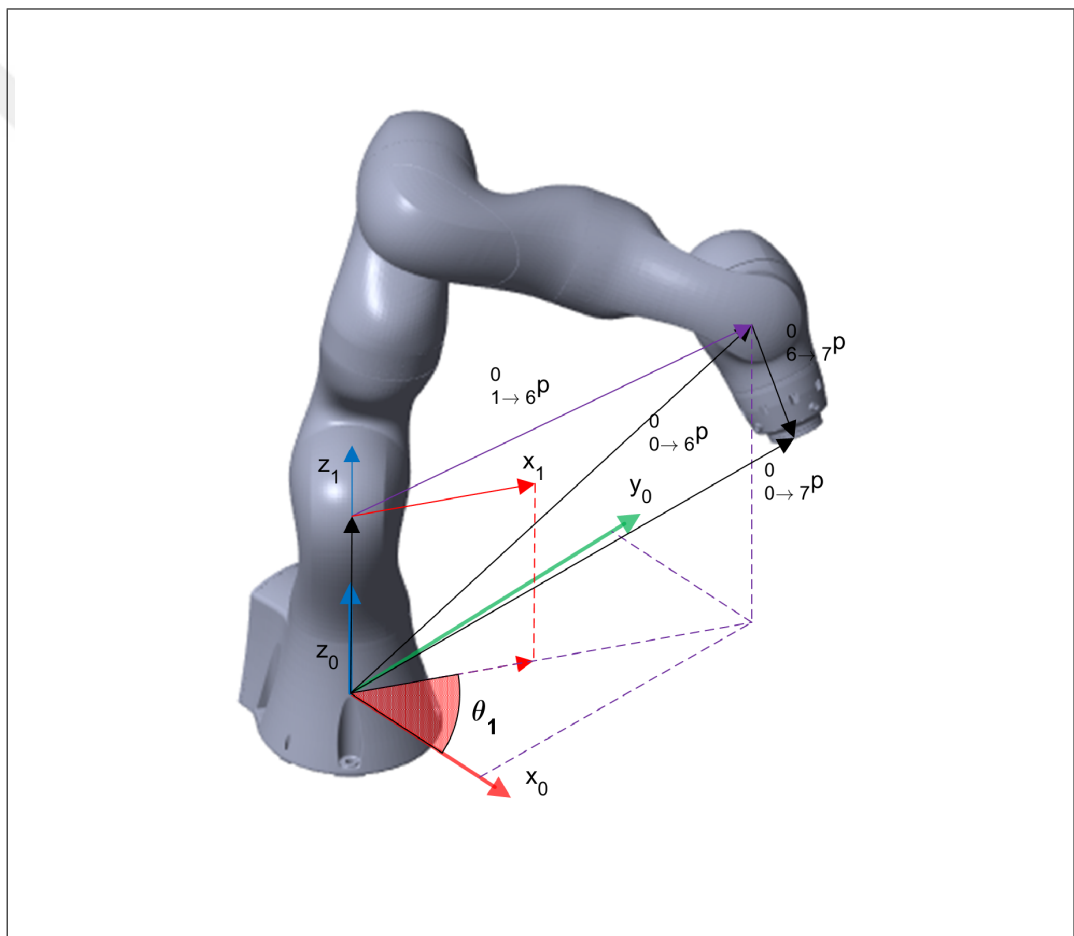
the base frame.

Note. 2: Any Vector with this form ${}^m_{i \rightarrow j} \vec{p}$ represents a vector p that starts from $i\vec{O}$ and ends at $j\vec{O}$ and is describes in Frame $\{m\}$.

3.2.1 Joint one

from figure 3.2 it can be realized that:

Figure 3.2: Geometric analysis regarding Joint angle θ_1 .



$${}^0_{0 \rightarrow 6} \vec{p} = {}^0_{0 \rightarrow 7} \vec{p} - {}^0_{6 \rightarrow 7} \vec{p} \quad (3.3)$$

and the vector ${}^0_{6 \rightarrow 7} \vec{p}$ can be calculated by:

$${}^0_{6 \rightarrow 7} \vec{p} = \hat{z}_7 \cdot d_7 \quad (3.4)$$

where ${}^0 \hat{z}_7$ is unit vectors of z axes of frame $\{7\}$.

Thus, using the components of ${}^0_{0 \rightarrow 6} \vec{p}$, a unique solution for angle θ_1 can be obtained in the form of:

$$\theta_1 = \text{atan2}({}^0_{0 \rightarrow 6} p_y, {}^0_{0 \rightarrow 6} p_x) \quad (3.5)$$

3.2.2 Joint four

referring to figure 3.3 The angle γ can be obtained by using the cosine rule in the triangle with the sides d_3, d_5 and ${}^0_{1 \rightarrow 6} \vec{p}$

$$\gamma = \arccos\left(\frac{d_3^2 + d_5^2 - \|{}^0_{1 \rightarrow 6} \vec{p}\|^2}{2d_3 d_5}\right) \quad (3.6)$$

And noticing that:

$$|\theta_4| = \gamma + 2\alpha \quad (3.7)$$

where

$$\alpha = \pi/2 - \gamma \quad (3.8)$$

$$\theta_4 = \begin{cases} \gamma - \pi \\ \pi - \gamma \end{cases} \quad (3.9)$$

The choice of θ_4 is up to the desired direction of the elbow joint. choosing the first solution results in the configuration illustrated in figure 3.4. Whereas figure 3.3 depicts the configuration that results from choosing the second solution. Also the choice of θ_4

affects the solution of joint angle θ_2 as it will be explained in the next section.

3.2.3 Joint two

Referring to the configuration illustrated in figure 3.3 (negative θ_4), and noticing that in this configuration θ_2 is negative, for this configuration the following equation holds true:

$$-\theta_2 = \beta - \phi \quad (3.10)$$

or

$$\theta_2 = \phi - \beta \quad (3.11)$$

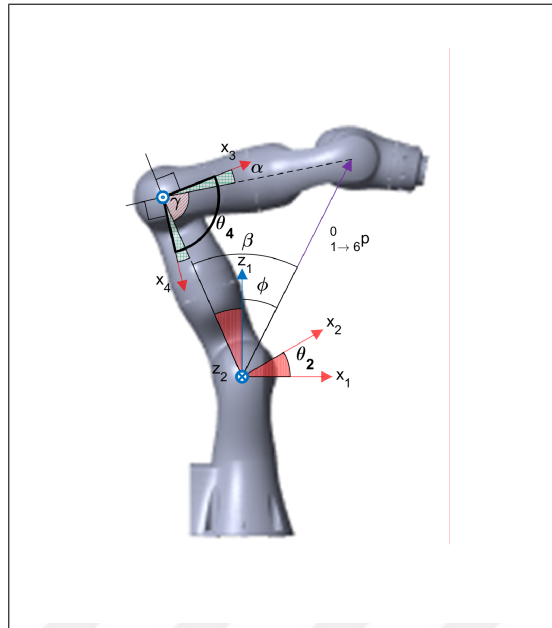
Where β is the angle between the sides d_3 and ${}^0_{1 \rightarrow 6}\vec{p}$ in the triangle with the sides: d_3, d_5 and ${}^0_{1 \rightarrow 6}\vec{p}$. Hence β can be obtained using the cosine rule:

$$\beta = \arccos\left(\frac{d_3^2 + \|{}^0_{1 \rightarrow 6}\vec{p}\|^2 - d_5^2}{2d_3 \|{}^0_{1 \rightarrow 6}\vec{p}\|^2}\right) \quad (3.12)$$

Notice that β is always positive, since it is measuring an interior angle of a triangle. Whereas ϕ takes negative and positive values depending on the output of the atan2 function :

$$\phi = \text{atan2}({}^1_{1 \rightarrow 6}p_x, {}^1_{1 \rightarrow 6}p_z) \quad (3.13)$$

Figure 3.3: Elbow left configuration.



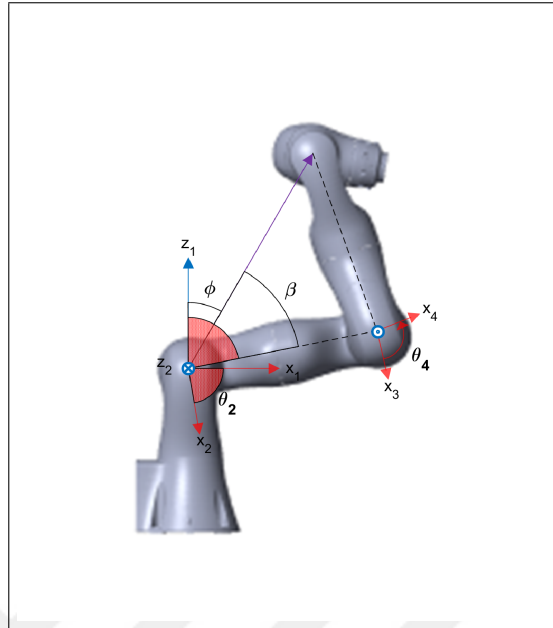
The other solution for θ_2 can be derived when a positive θ_4 (figure 3.4) is chosen, this choice results in a different formula for calculating θ_2 :

$$\theta_2 = \beta + \phi \quad (3.14)$$

Hence

$$\theta_2 = \begin{cases} \phi + |\beta| \\ \phi - |\beta| \end{cases} \quad (3.15)$$

Figure 3.4: Elbow right configuration
 θ_1 .



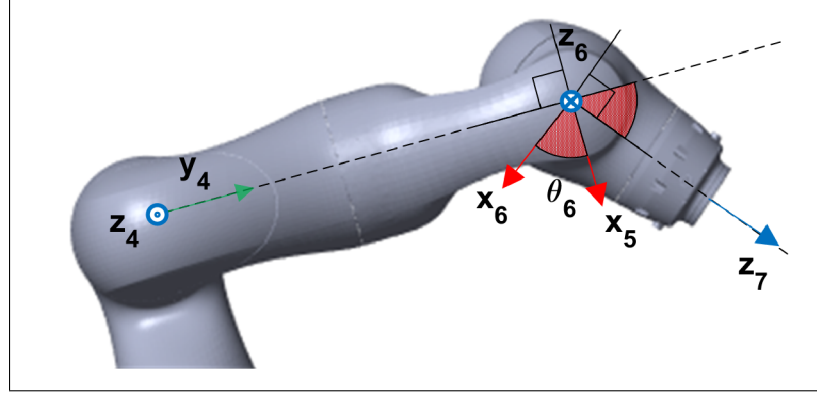
3.2.4 Joint six

From figure 3.5, it can be noticed that joint angle θ_6 is equal to the angle between the unit vectors \hat{y}_4 and \hat{z}_7 , hence, by using the dot product of these two vectors, θ_6 can be obtained from:

$$\theta_6 = \arccos((\hat{y}_4) \cdot (\hat{z}_7)) \quad (3.16)$$

Notice that since the dot product is used, the solution joint angle θ_6 is unique and takes values within the range 0 to π

Figure 3.5: Geometrical analysis regarding joint angle six.



3.2.5 Joints five and seven

Since $\theta_1, \theta_2, \theta_3$ and θ_4 are all available ${}^0\mathbf{R}$ can be computed using forward kinematics, hence 4_7R can be calculated in the form of:

$${}^4_7R = {}^4_0R {}^0_7R = \begin{bmatrix} r_{11} & r_{12} & r_{13} \\ r_{21} & r_{22} & r_{23} \\ r_{31} & r_{32} & r_{33} \end{bmatrix} \quad (3.17)$$

Where r_{ij} are the numeric values of ${}^4_7\mathbf{R}$.

On the other hand, ${}^0_4\mathbf{R}$ can also be obtain symbolically using forward kinematics as well.

The result is:

$${}^4_7R = \begin{bmatrix} c_5c_6c_7 - s_5s_7 & -c_7s_5 - c_5c_6s_7 & c_5s_6 \\ -c_7s_6 & s_6s_7 & c_6 \\ -c_6c_7s_5 - c_5s_7 & c_6s_5s_7 - c_5c_7 & -s_5s_6 \end{bmatrix} \quad (3.18)$$

Thus, the solution of θ_5, θ_7 yields to :

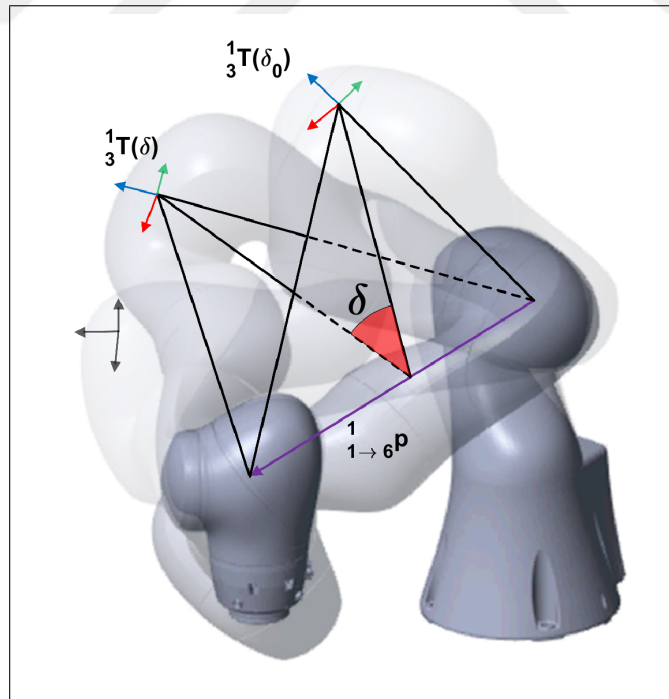
$$\theta_5 = \text{atan2}(-r_{33}, r_{13}) \quad (3.19)$$

$$\theta_7 = \text{atan2}(r_{22}, -r_{21}) \quad (3.20)$$

3.3 POSTURE KINEMATICS

A redundant serial manipulator with a similar kinematic structure to LBR IIWA possess the ability to change its posture and maintain the desired transformation of the end-effector simultaneously. In practice this feature can be accomplished by rotating the elbow with an angle δ about the axis that connects center of the shoulder and center of the wrist as illustrated in figure 3.6.

Figure 3.6: The geometry of posture motion.



Mathematically, such rotation can be described using angle axis rotation matrix $R(\delta, \frac{1}{1 \rightarrow 6} p)$ (Craig, 2005, pp.47). If frame 3 is chosen to represent the elbow rotation, then the desired transformation of the elbow frame can be calculated from :

$${}^1_3\mathbf{T}(\delta) = \left[\begin{array}{ccc|c} \mathbf{R}(\frac{1}{1 \rightarrow 6}\mathbf{p}, \delta) & \mathbf{0} & & \\ \hline 0 & 0 & 0 & 1 \end{array} \right] \cdot {}^1_3\mathbf{T}(\delta_0) \quad (3.21)$$

Where $\delta_0 = 0$, implying that ${}^1_3\mathbf{T}(\delta_0)$ is the initial transformation of the elbow frame which is when the robot places the elbow according to required 6-Dof Solution. Thus, a function that maps the elbow angle to the elbow frame is established. As a result, The input of the robot can be extended to include the elbow angle δ . However, it should be pointed this function implies that the 6-DoF inverse kinematics solution is solved so that $\frac{1}{1 \rightarrow 6}\mathbf{p}$ and ${}^1_3\mathbf{T}(\delta_0)$ are available.

3.3.1 7-DOFS INVERSE KINEMATICS SOLUTION

As explained earlier, The redundancy solution is concern only with the elbow motion, and realizing that this motion is irrelevant to the elbow joint (joint four), hence, the value of this joint remains unchanged as calculated in section 3.2. Thus, the problem is reduced to 6-Dofs only. Hence, given the Desires elbow frame transformation ${}^1_3\mathbf{T}(\delta)$ and the solution of the 6-Dof inverse kinematics, The new joint angles including the redundant joint must be found.

Referring to figure 3.8, joint one can be found using the angular displacements $\Delta\theta_1$:

$$\theta_1 = \Delta\theta_1 + \theta_1(\delta_0) \quad (3.22)$$

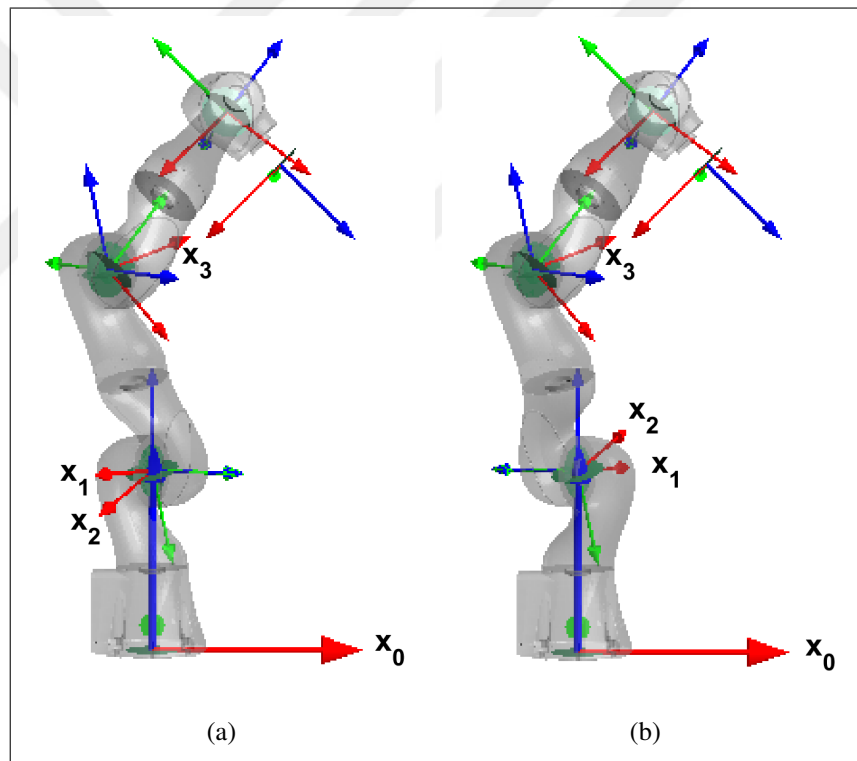
Where

$$\Delta\theta_1 = \text{atan2}(\frac{1}{1 \rightarrow 3}p_y, \frac{1}{1 \rightarrow 3}p_x) \quad (3.23)$$

Although mathematically the solution is correct, practically, this solution results in an unnecessary high value of joint rotation for the global configuration chosen for the surgical task. Referring to figure 3.7(a), notice that joint one and three are 'flipped' 180 Degree to obtain the desired configuration. Instead, it is better to flip the reference coordinate system that is used to calculate $\Delta\theta_1$, this can be done by reversing the sign of ${}^1_{1\rightarrow3}p$ components :

$$\Delta\theta_1 = \text{atan2}(-{}^1_{1\rightarrow3}p_y, -{}^1_{1\rightarrow3}p_x) \quad (3.24)$$

Figure 3.7: An example configuration to illustrate Joints 1 and 3 flipping problem. (a) Non-reversed coordinates, $\theta_1 = 122$ and $\theta_3 = 160$ Degree. (b) Reversed coordinates, $\theta_1 = 58$ and $\theta_3 = -20$ Degree



Joint angle θ_2 can be obtained from

$$\phi = \text{atan2}({}^1_{1\rightarrow3}p_z, {}^1_{1\rightarrow3}p_x) \quad (3.25)$$

$$\theta_2 = \pi/2 - \phi \quad (3.26)$$

Joint angles θ_3 and can be obtained algebraically by realizing 2_3R , this is possible because θ_1 and θ_2 are available which will give 2_0R using forward kinematics, and 0_3R which is the rotation matrix that is given by the secondary task already. Hence

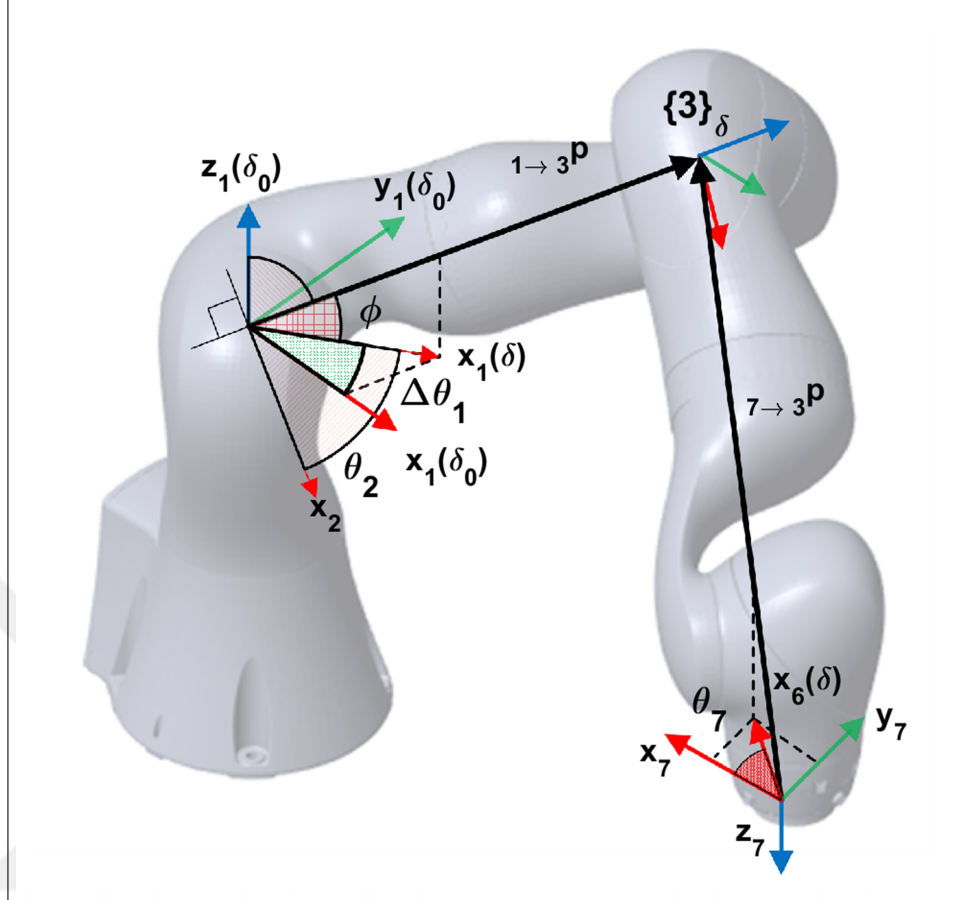
$${}^2_3R = {}^2_0R {}^0_3R \quad (3.27)$$

Symbolically

$${}^2_3R = \begin{bmatrix} c_3 & -s_3 & 0 \\ 0 & 0 & -1 \\ s_3 & c_3 & 0 \end{bmatrix} \quad (3.28)$$

$$\theta_3 = \text{atan2}(r_{31}, r_{11}) \quad (3.29)$$

Figure 3.8: The geometrical analysis of joint angles one and seven.



Joint angles θ_5, θ_6 and θ_7 can be obtained using the equations Eq. (3.19), (3.16) and (3.20) respectively that are previously found in the task space kinematics. However, 4_7R must be recalculated from forward kinematics since now θ_3 is not zero anymore. Another approach to find Joint angle θ_7 is geometrically by using the components of the vector connecting the end-effector to the elbow (figure. 3.8) :

$$\theta_7 = -\text{atan2}({}^7_{7 \rightarrow 3} p_y, {}^7_{7 \rightarrow 3} p_x) \quad (3.30)$$

3.4 REDUNDANCY RESOLUTION

In this section, an algorithm is proposed to avoid joint limits. the input to this algorithm is the joint angles calculated by the 6-DoF kinematic solution, The output must be the optimal arm angle that places the joints in the furthest distance from their limits.

Faria et al. (2018) Suggested a method to avoid joint limits and singularities using the rotation of the arm angle. Their method depends on finding the regions where the arm angle does not hit a limit or a singular configuration, such regions are termed "feasible intervals". Thus, the motion is optimized by locating the arm angle in the middle of a feasible interval. They propose using a potential filed to relocate the arm angle to its optimum position. This results in a sluggish transition to the optimum, consequently, the primary task might hit a joint limit before the arm angle converges to the optimum.

On the other hand, In this thesis, firstly, an exponential score function is proposed to quantify the quality of a configuration in terms of its distance from joint limits. Utilizing the score function, two local search algorithms are proposed. The first one converges to the optimum configuration by iterative search and evaluation of possible optimum configurations. This algorithm converges once a score threshold value is met. Whereas in the second algorithm, instead of obtaining the optimum arm angle, the algorithm gradually descends or ascends to the optimum. Both algorithms are tested on a simulation environment and on the real robot.

3.4.1 Score Function

The algorithm decides the optimal arm angle based on a score function that takes the following form

$$S = e^{-C} \tag{3.31}$$

Where C is a cost function proposed by (Yu et al., 2012):

$$C = \sum_{i=1}^7 \frac{(\theta_{i\max} - \theta_{i\min})^2}{(\theta_{i\max} - \theta_i)(\theta_i - \theta_{i\min})} \quad (3.32)$$

The advantages of this cost function are that it amplifies the cost of the joints which are close to their limits. However, if we plot the cost as a function to arm angle for an arbitrary configuration, we will realize that it suffers from discontinuity and local minima as illustrated in figure 3.9. This characteristic is not convenient for search algorithms as they might converge to a local minimum. Therefore it is necessary to find a function that is continuous, linear or close to linear and does not suffer from local minima. Such function can be found by using equation 3.31, The result is depicted in figure 3.10.

Figure 3.9: The polar plot of the cost as it varies with the arm angle δ . The star represents the global minimum at which δ is optimal.

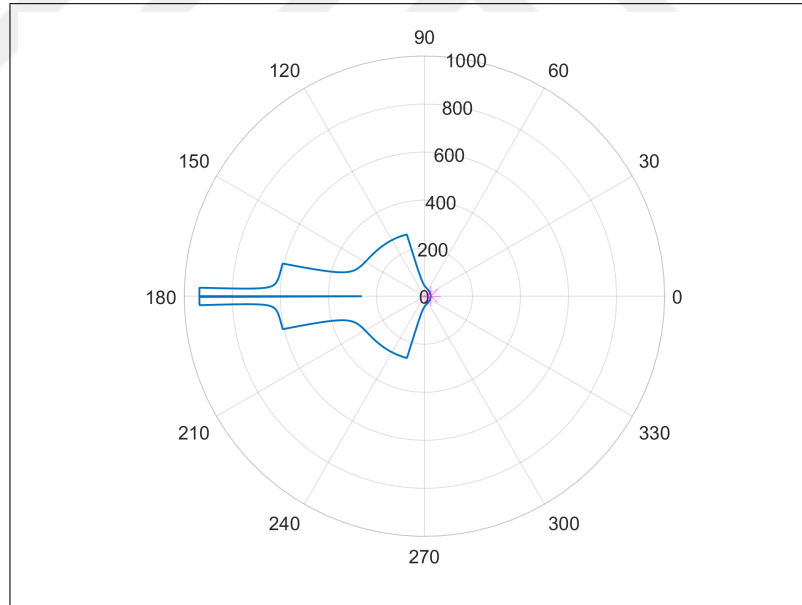
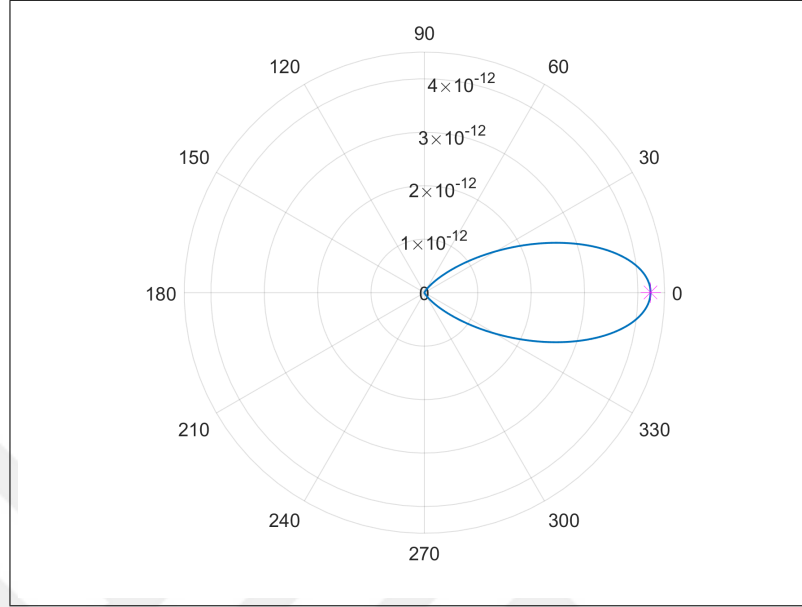


Figure 3.10: The polar plot of the exponential scores for each value of arm angle δ . The star represents the global maximum at which δ is optimal.



As can be seen from figure 3.10, the desired characteristic is obtained, however, the score function outputs very small values that are due to using the unnormalized cost function that outputs extremely high values. Therefore the cost function must be normalized. To avoid an infinite cost in the normalization procedure, joint angles must not reach their exact limits, assuming that each joint has an upper positive limit and a lower negative limit (which is the case in KUKA IIWA) the following saturation function can be used:

$$\theta_i = \begin{cases} \theta_{i\max} - \epsilon & \text{if } \theta_i \geq \theta_{i\max} - \epsilon \\ \theta_{i\min} + \epsilon & \text{if } \theta_i \leq \theta_{i\min} + \epsilon \end{cases} \quad (3.33)$$

If we choose ϵ to be 0.0175 Radian (1 Degree) the normalizing factor of joint one, for example, will be

$$C_1 = \frac{(\text{Rad}(170) - \text{Rad}(-170))^2}{((\text{Rad}(170) - \text{Rad}(169))(\text{Rad}(169) - (\text{Rad}(-170))))} \quad (3.34)$$

Thus the normalization factor of joints 1,3 and 5 (since they have the same joint limits) is

$$n_{f1,3,5} = \frac{1}{341.0029} \quad (3.35)$$

Normalization factors for other joints can be obtained in a similar fashion. Hence, the cost can be normalized:

$$C_n = \frac{(C_1 + C_3 + C_5)n_{f1,3,5} + (C_2 + C_6)n_{f2,6} + C_7n_{f7}}{N - 1} \quad (3.36)$$

where N is the number of joints, notice that we excluded joint four from cost calculation due to the fact that the motion of this joint is independent of the arm angle.

By plotting the score of the normalized cost function (figure 3.11) it can be realized that firstly, the scores are not taking extremely high values. Secondly, the score function covers more range of arm angle with a non zero score which a good characteristic for search algorithms. however, it is noticed that the local minima and discontinuous region appear again after the normalization. Such a problem can be solved by multiplying the exponent by a tinning factor λ

$$S = e^{(-C_n\lambda)} \quad (3.37)$$

Now we can tune the score function by changing λ .Figure 3.12(a)

Figure 3.11: The polar plot of the exponential scores for each value of arm angle δ . The star represents the global maximum at which δ is optimal.

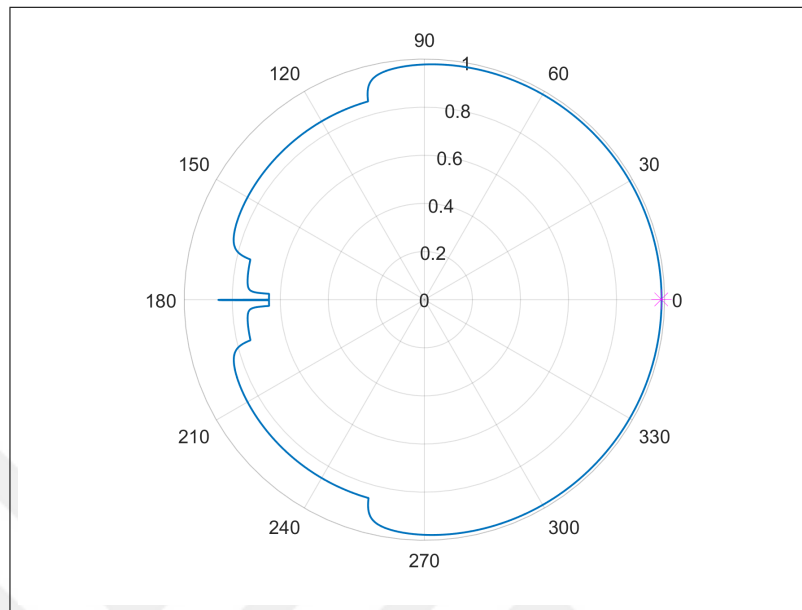
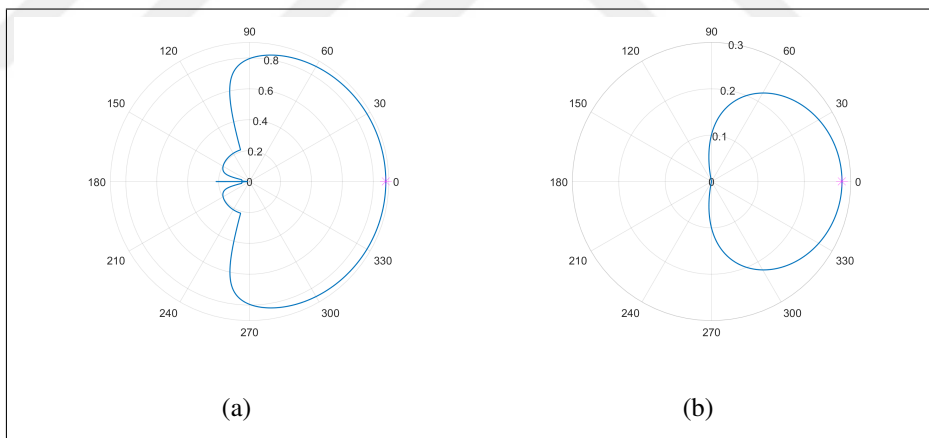


Figure 3.12: Tuning the score function (a) $\lambda = 10$. (b) $\lambda = 100$.



3.4.2 Experimental Analysis

To generalize the validity of the score function, multiple experiments are performed for different configurations of the robot. It should be pointed out that these experiments are performed within the scope of the global configuration that is suitable to the surgical

platform. In other words, the aim of this analysis is to find a common rule to search for the optimal arm angle based on the proposed score function.

The experiments are performed as follows:

- (i) Four configurations are chosen, A and A' represent motion on the X Y plane, and requires motion of the pivot joints (1,3,5,7). The other two configurations are B and B', which represents motion on X Z plane and requires motion of the hinge joints (2,4,6).
- (ii) For each configuration, the arm angle δ is given continuous values from 0 to 360 Degrees and the score of each value is recorded.
- (iii) A polar plot for the angle and the score is visualized and the optimum angle is the one with the highest score.
- (iv) Finally, command the robot to go to the optimal angle.

Figures 3.13, 3.14, 3.15 and 3.16 depicts the experiments. It can be realized that the function reflects the symmetry of the configuration, A and A' are symmetrical and so their scores. The other interesting result is that B and B' can not be optimized further, this means that in the RCM motion around the trocar, only the angle that requires motion on X Y plane can be increased through arm angle optimization. It is also noticed that the function preserve continuity for different configuration and has one global maximum most likely in the region between -90 and 90 Degree. Therefore a local search algorithm can be used to find the global maximum.

Figure 3.13: Optimization of configuration A by rotating the arm angle.(a) initial configuration .(b) optimized configuration.(c) Score function with the optimal arm angle represented by the red circle.

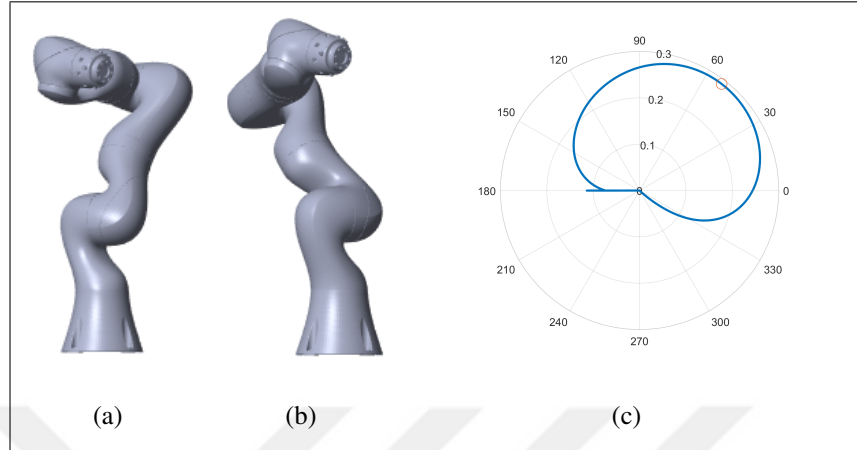


Figure 3.14: Optimization of configuration A' by rotating the arm angle.(a) initial configuration .(b) optimized configuration.(c) Score function with the optimal arm angle represented by the red circle.

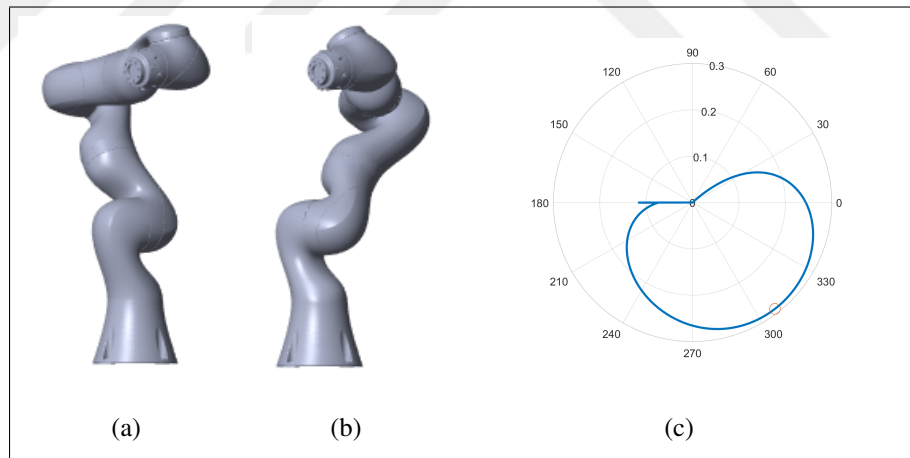


Figure 3.15: Optimization of configuration B by rotating the arm angle.(a) initial configuration .(b) optimized configuration.(c) Score function with the optimal arm angle represented by the red circle.

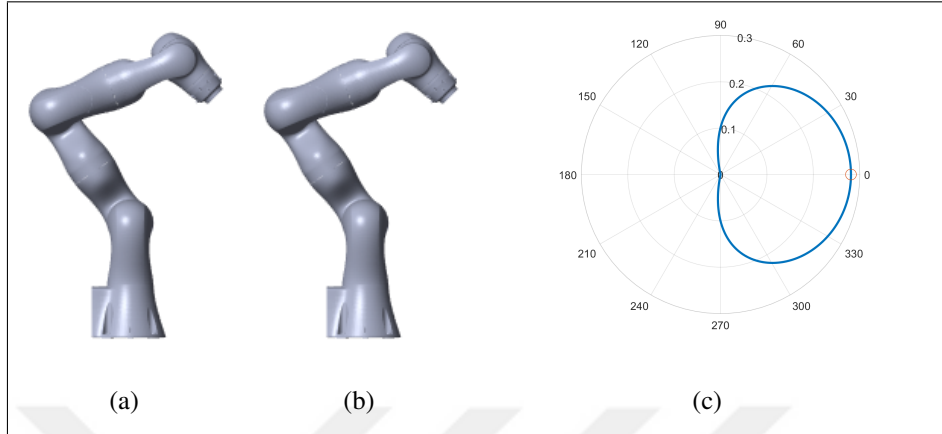
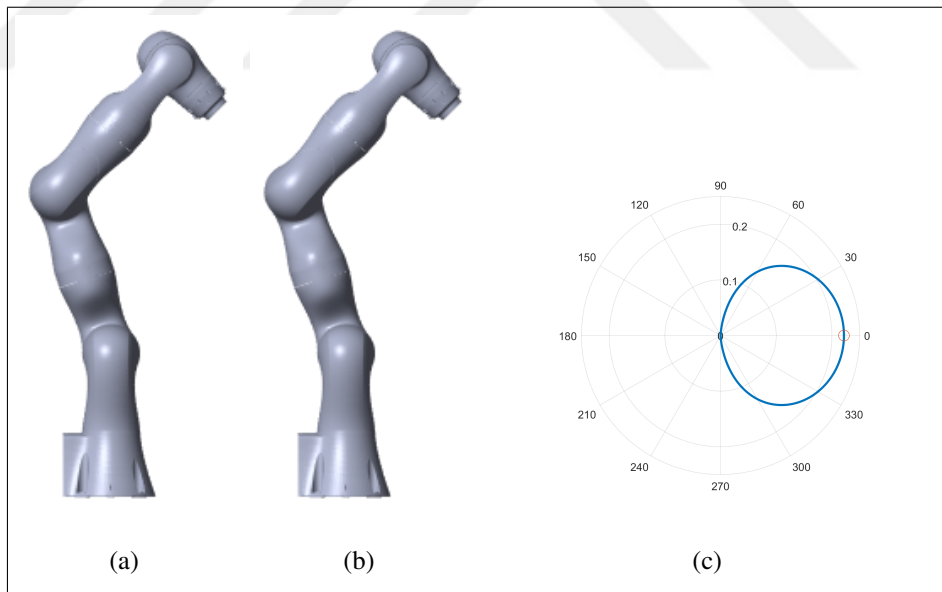


Figure 3.16: Optimization of configuration B' by rotating the arm angle.(a) initial configuration .(b) optimized configuration.(c) Score function with the optimal arm angle represented by the red circle.



3.4.3 Iterative Optimization Algorithm

The aim of THIS search algorithm is to find the optimal arm angle with the least computations. This is necessary for motion planning in real time. As seen from the previous section, a global maximum is most likely lies within the range of 90 and -90 Degree. Utilizing the enhanced score function, an Iterative Optimization Algorithm is used. The algorithm steps are as follows:

- (i) Chose two angles angle A and angle B.
- (ii) Let A be the upper limit of the search range 90 Degree and B the lower limit B -90 Degree.
- (iii) Find the scores of A and B.
- (iv) Calculate the angular distance between A and B

$$Dist = A - B \quad (3.38)$$

- (v) If $Score_A \geq Score_B$ increase B:

$$B \leftarrow B + Dist \times Step \quad (3.39)$$

Where

$$Step = \frac{Score_A}{Score_A + Score_B} \mu \quad (3.40)$$

Assuming that the cost function is linear, $\mu = 1$, if that is not the case, the step might overshoot the optimum, thus μ can be tuned manually by trial and error, in our case $\mu = 0.8$.

Update $Score_B$ that corresponds to the new value of B.

If $Score_A < Score_B$ reduce B:

$$A \leftarrow A - Dist \times Step \quad (3.41)$$

Update $Score_A$ that corresponds to the new value of A.

(vi) Update The angular distance.

(vii) If $|Dist| \leq Threshold$

$$\delta_{optimum} = \frac{A + B}{2} \quad (3.42)$$

Else, go back to Step V.

3.4.4 Iterative Optimization Algorithm Experiments

Firstly, the algorithm is tested statically on predefined configurations (A' and B'). The algorithm converged after 6 iterations for both configurations. This is an important result as it means that If the control frequency of the primary task is f the frequency of arm angle control for optimization will be $\frac{f}{6}$. The results are illustrated in Table 3.2 and 3.3, Figures 3.17 and 3.18.

Table 3.2: Algorithm validation. Angles are measured in Degree

Configuration	Iterations	Result	Optimum	$ Error $
A'	6	-55.3377	-52.3	3
B'	6	-0.404506	0	0.4

Table 3.3: Comparison of joint angles before and after the optimization

	A'	A' Optimized	Joint Limit +/-
Joint 1	34.6370	-37.5149	170
Joint 2	-33.7344	46.6308	120
Joint 3	0	26.8722	170
Joint 4	-114.5648	-114.5648	120
Joint 5	-81.2033	-35.0525	170
Joint 6	80.5582	40.6277	120
Joint 7	-3.4580	-30.8504	175

Figure 3.17: The algorithm convergence for configuration A'.

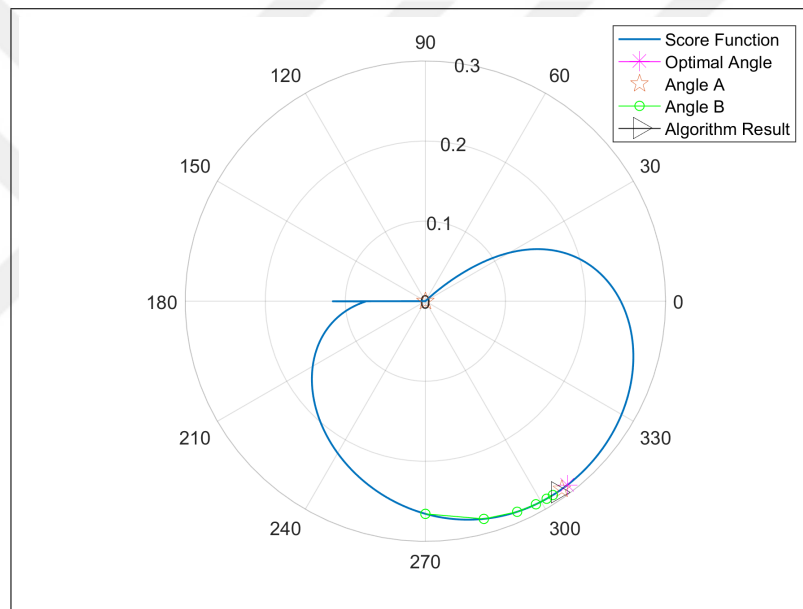
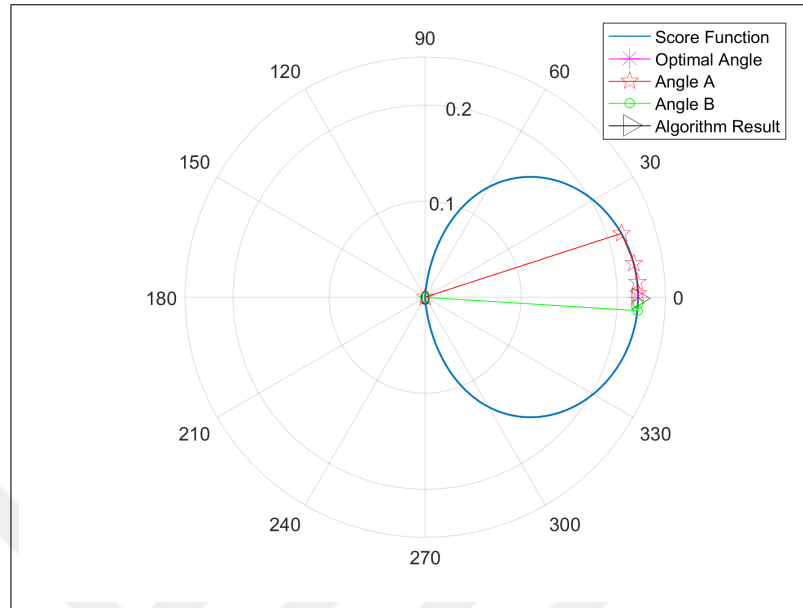


Figure 3.18: The algorithm convergence for configuration B' .



Also, the algorithm is implemented in C++ in order to test its performance in real time. Because the primary task is faster than the secondary task, we avoided using a cascaded controller, instead, using concurrent programming, the primary task runs with its control frequency f , the process that handles the algorithm, updates the arm angle each $\frac{f}{\text{Number of iterations}}$.

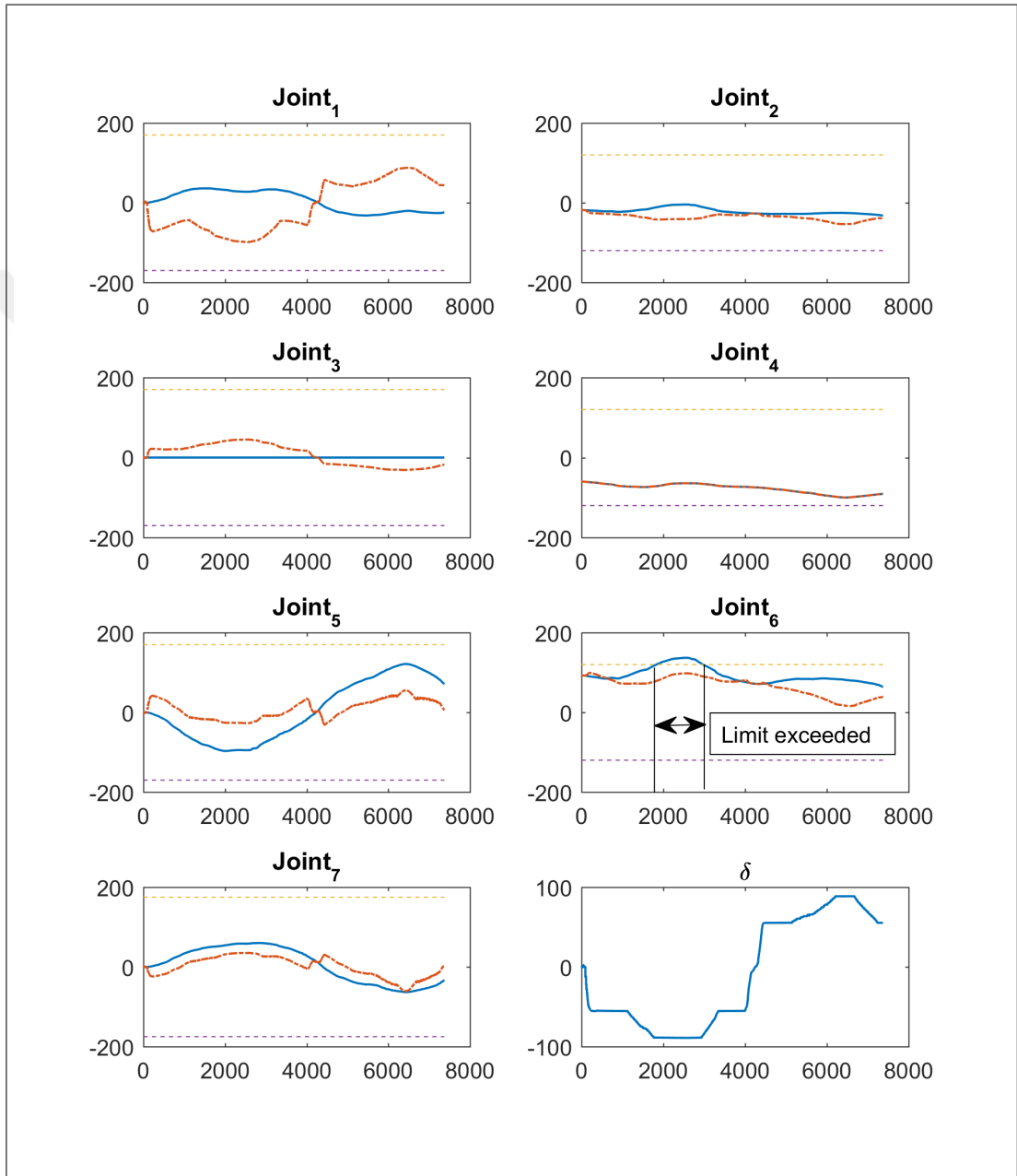
An experiment is performed to test real-time optimization. The operator is commanding the primary task using the haptic controller Omega.6, meanwhile, a process running in the background that updates the current configurations based on the convergence of the search algorithm. A video of the non-optimized¹ and optimized² motion control is provided. The joint space trajectory of the 6-DoF unoptimized and 7-DoF optimized motion is recorded while executing the same task space trajectory and compared as illustrated in figure 3.19. It can be noticed from the data that $joint_6$ limit is exceeded in the trajectory of the unoptimized motion. whereas, this joint limit is avoided in the optimized 7-DoF

¹<https://youtu.be/aEqtG7Vhfoc>

²<https://youtu.be/4AaVDS9Nbu8>

trajectory.

Figure 3.19: Real-time joint limit avoidance. The blue line represents the 6-DoF joint trajectory. While the dashed red line represents the 7-DoF joint trajectory. The upper and lower limit of each joint is represented by the dotted lines. The x axis is the time in milliseconds.



3.4.5 Hill Climbing Algorithm

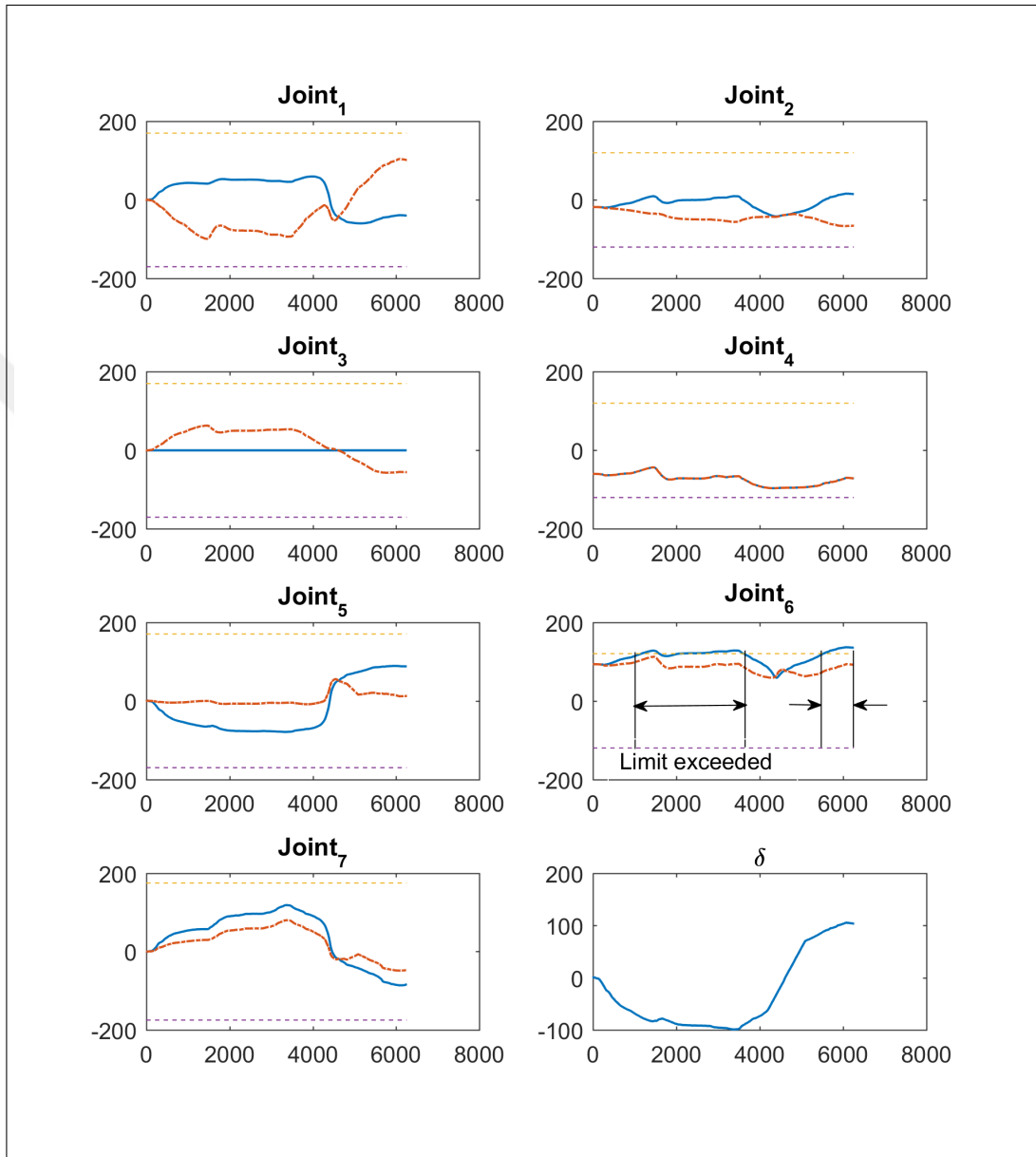
As seen in the experimental analysis section, the score function is continuous with one global maximum, thus If we chose a small neighborhood around the current the current arm angle $[\delta_{t-1} - \epsilon, \delta_{t-1} + \epsilon]$ where ϵ is a positive non-zero real number. We can examine the score of the limits of this neighborhood and chose the limit with the higher score to be the commanded arm angle δ_t . Mathematically :

$$\delta_t = \begin{cases} \delta_{t-1} + \epsilon & \text{if } S(\delta_{t-1} + \epsilon) > S(\delta_{t-1} - \epsilon) \\ \delta_{t-1} - \epsilon & \text{if } S(\delta_{t-1} + \epsilon) < S(\delta_{t-1} - \epsilon) \\ \delta_{t-1} & \text{if } S(\delta_{t-1} + \epsilon) = S(\delta_{t-1} - \epsilon) \end{cases} \quad (3.43)$$

Notice that this algorithm does not necessarily find the optimum of the current configuration. However, it moves the robot gradually to the optimum arm angle, thus the secondary task is updated in much faster rate than in the previously discussed algorithm. This tiny gradual transition toward the optimum arm angle is a very important behavior in real-time control of the real robot, because it mitigates the sudden changes in joint positions in case of directly commanding the optimum angle.

The algorithm is implemented in a C++ based simulation environment (Chai3d). An experiment is conducted to evaluate the performance. In the experiment, the user operates the robot through the haptic device Omega.6. The joint values are recorded for both redundant and non-redundant inverse kinematic solution and illustrate in figure 3.20 together with the arm angle δ . The data shows that the algorithm succeeded in avoiding *joint*₆ limits. Moreover, the profile of the arm angle δ is much smoother than the one produced in the Iterative Optimization approach. To test the algorithm on the real robot, the simulation data are filtered with a low pass filter and commanded to the real robot. The robot approaches a joint limit in the 6-DoF motion, while it avoids the joint limit in the optimized motion.

Figure 3.20: Real-time joint limit avoidance using the Hill Climbing Algorithm . The blue line represents the 6-DoF joint trajectory. While the dashed red line represents the 7-DoF joint trajectory. The upper and lower limit of each joint is represented by the dotted lines. The x axis is the time in milliseconds.



4. KUKA IIWA DYNAMIC ANALYSIS

4.1 INTRODUCTION

with the mindset shift that occurred among governments and business leaders towards Post-automation era, new technologies have and still being developed to cope with the fourth industrial revolution (Industry 4.0). As a matter of fact, the industrial intelligent work assistant robot (IIWA) was developed by Kuka intentionally to cover the demanding market of collaborative robots which is a major sector envisioned by industry 4.0. indeed, the robot is well equipped to collaboratively work side by side with factory workers, for example, each joint is provided with a highly sensitive torque sensors working together with a permanent monitoring system (PMS) to detect and avoid potential hazardous collision .

Evolved originally from its ancestor the anthropomorphic lightweight KUKA LBR, IIWA was manufactured to meet the agility of LBR and the robustness of transitional industrial robots. both robots have the same kinematic structure yet, IIWA weighs almost triple the weight of LBR making them have a different dynamic characteristic. a side of mechanical properties a substantial disadvantage of IIWA is the restrictions Kuka have had on their software which prevents the user from having access to the manipulator's mass matrix, unlike LBR witch grants a full access to all configuration dependent terms (mass matrix, gravity vectro, jacobian)(Gaz et al., 2014). consequentially, the absence of these terms will hinder implementation of end effector dynamic behavior based control methods (Khatib, 1987), due to their dependency on the end-effector equation of motion. Furthermore, gravity compensation mode is not available on IIWA, a work around to this problem is either to run the manipulator on impedance control mode and set joints stiffness to zero, or to run it on "joint torque overlay" mode using the Fast Robot Interface (FRI) witch is an interface for real time applications. However, in both cases the controller fails to accurately compensate for the gravity causing the arm to drift from its desired configuration.

Numerous algorithms, suitable for simulation and real-time control, exist for numerically computing the dynamic parameters of robot manipulators. Most notably, algorithms such as the Articulated Body Algorithm (ABA) Featherstone (1983) and the Recursive Newton-Euler Algorithm (RNEA) (Featherstone & Orin, 2000) are computationally efficient for obtaining the inverse and forward dynamics, respectively. However, these methods do not provide the mass matrix and therefore are not suitable for operational-space control. The Composite Rigid Body Algorithm (CRBA) (Featherstone & Orin, 2000) calculates the mass matrix but requires up to four nested loops and thus, has high computational complexity. Lilly and Orin (Lilly & Orin, 1991) proposed the Structurally Recursive Method (SRM) algorithm for the computation of the mass matrix. Unlike ABA and RNEA, SRM uses link Jacobians to calculate the mass matrix. Consequently, the SRM eliminates the need to separately compute the Jacobian matrix. Although this approach is very useful, it doesn't provide the gravity vector, which is essential for most robotic applications.

Therefore, the objective of this chapter is

- (i) providing IIWA's mass matrix and gravity vector in real time through a simple algorithm based on structurally recursive algorithm.
- (ii) This algorithm will be used to estimate the external forces acting IIWA's end effector.

4.2 DYNAMIC MODELING

The general equation of motion of an N -DOF robotic manipulator is given as

$$\mathbf{M}(\mathbf{q})\ddot{\mathbf{q}} + \mathbf{c}(\dot{\mathbf{q}}, \mathbf{q}) + \mathbf{g}(\mathbf{q}) + \mathbf{J}^T \mathbf{F}_{\text{ext}} = \mathbf{\Gamma} \quad (4.1)$$

where $\mathbf{M}(\mathbf{q})$ is the $(N \times N)$ inertia matrix, $\mathbf{c}(\dot{\mathbf{q}}, \mathbf{q})$ and $\mathbf{g}(\mathbf{q})$ are the $(N \times 1)$ centripetal

force and gravity vectors, respectively, \mathbf{J} is the $(6 \times N)$ Jacobian, \mathbf{F}_{ext} is the (6×1) vector of external forces and moments acting on the end-effector, $\mathbf{\Gamma}$ is the $(N \times 1)$ joint torques, $\mathbf{q} = [\theta_1, \theta_2, \dots, \theta_N]^T$ is the $(N \times 1)$ vector of joint variables, and $(\cdot)^T$ indicates the matrix transpose. The inertia matrix can be derived using the Lagrangian approach as W. et al. (2004)

$$\mathbf{M} = \sum_{i=1}^N \mathbf{J}_{c_i}^T \mathcal{M}_i \mathbf{J}_{c_i} \quad (4.2)$$

where \mathcal{M}_i is the (6×6) positive definite symmetrical matrix termed generalized inertia matrix and contains the inertial properties (*i.e.*, mass and inertia tensor) of link i referenced with respect to the body frame of the associated link W. et al. (2004). In addition, \mathbf{J}_{c_i} is the Jacobian between the base frame and the body frame of link i . In this study, the inertia values are taken from two different sources: 1) the KUKA CAD files and 2) values published by Stürz *et. al.* (2017). If the manipulator is undertaking slow motion with small joint angular velocities, the centripetal force term will have a small affect in the robot dynamics and can be ignored.

The gravity vector \mathbf{g} can be obtained by treating the gravitational forces acting on each link as external forces exerted on that link's COM. Since the gravitational forces are always along the z_0 -axis (*i.e.*, base frame z -axis), the gravitational force vector for link i is expressed as a (6×1) vector in the form of $\mathcal{G}_i = [0 \ 0 \ m_i g \ 0 \ 0 \ 0]^T$ Where m_i is the mass of link i and $g = -9.81 \text{ m.s}^{-2}$ is the gravitational acceleration. The gravitational joint torques corresponding to the weight of the i^{th} link can be obtained by projecting the \mathcal{G}_i vector into joint space using \mathbf{J}_{c_i} in the form of $\mathbf{g}_i = \mathbf{J}_{c_i}^T \mathcal{G}_i$. Finally, the joint torques necessary for overcoming the weight of the manipulator is computed by summing up the contribution of each link as

$$\mathbf{g} = \sum_{i=1}^N \mathbf{g}_i = \sum_{i=1}^N \mathbf{J}_{c_i}^T \mathcal{G}_i. \quad (4.3)$$

4.3 THE PROPOSED ALGORITHM

In this section, an algorithm for recursively computing the pertinent dynamic parameters (*i.e.*, mass and Jacobian matrices, and the gravity vector) of a robot manipulator is proposed.

The algorithm consist of two nested loops and a separate computations step. The outer loop starts from link 1 and iterates up to link N . Each iteration involves the following three steps:

Step 1: Outward Iterations - Computation of the COM positions

- (a) Recursively calculate the homogeneous transformation for link i at the current sample time t with respect to the base using equation 3.1
- (b) Compute the COM vector of link i with reference to the base frame using the previously calculated homogeneous transformation

$${}^0\mathbf{o}_{c_i} = {}^0_i\mathbf{T} \cdot ({}^i\mathbf{o}_{c_i}). \quad (4.4)$$

Step 2: Inward Iterations - Computation of the COM Jacobian

- (i) The computation of the Jacobian of the COM of link i can be performed as a part of an inner loop. For each intermediate link k such that $1 \leq k \leq i$, the k^{th} column of the corresponding link Jacobian is computed as

$$\mathbf{J}_{c_i,k} = \begin{bmatrix} {}^0\mathbf{z}_k \times ({}^0\mathbf{o}_{c_i} - {}^0\mathbf{o}_k) \\ {}^0\mathbf{z}_k \end{bmatrix} \quad (4.5)$$

where ${}^0\mathbf{z}_k$ is the joint axis of frame $\{k\}$ and ${}^0\mathbf{o}_k$ is the origin of frame $\{k\}$ described in the base frame. Although not explicitly labeled, the COM Jacobian \mathbf{J}_{c_i} is defined with respect the the base frame $\{0\}$. It should be noted that (4.5) is only valid for

links connected through revolute joints. However, a similar equation can also be derived for prismatic joints [add Spong reference]. Both \mathbf{z}_k and ${}^0\mathbf{o}_k$ are the third and the fourth columns of the previously calculated link transformation, respectively excluding the homogeneous part.

For example, after the completion of Step 1 (outward loop) for link $i = 3$, the position vectors of the first three link frames (*i.e.*, ${}^0\mathbf{o}_1$, ${}^0\mathbf{o}_2$, and ${}^0\mathbf{o}_3$) and the position vectors of the first three COMs referenced with respect to the base frame (*i.e.*, ${}^0\mathbf{o}_{c_1}$, ${}^0\mathbf{o}_{c_2}$, and ${}^0\mathbf{o}_{c_3}$) will be computed and available for the inward iterations. As k takes on values from 1 to i , the inward loop will iterate three times; each iteration will result in the k^{th} column of the Jacobian ${}^0\mathbf{J}_{c_3,k}$. Stacking these columns side-by-side will yield ${}^0\mathbf{J}_{c_3}$ in the form of

$$\mathbf{J}_{c_3} = \begin{bmatrix} \mathbf{J}_{c_3,1} & \mathbf{J}_{c_3,2} & \mathbf{J}_{c_3,3} & \mathbf{0} & \mathbf{0} & \mathbf{0} & \mathbf{0} \end{bmatrix} \quad (4.6)$$

where $\mathbf{0}$ indicates a matrix/vector of zeros of appropriate dimension.

Step 3: Computation of Dynamic Parameters

- Once the COM Jacobians \mathbf{J}_{c_i} are computed, the mass matrix \mathbf{M} and gravity vector \mathbf{g} are computed using (4.2) and (4.3).

The pseudo-code of the proposed ESRA is provided in algorithm 1:

4.4 EXPERIMENTS AND VALIDATION

Since joint velocities and accelerations on the KUKA LBR IIWA are not accessible, validating the proposed algorithm is by itself challenging. For this purpose, two different experiments are designed and conducted. Initially, the numerical simulation software Simscape MultibodyTM is used to validate the dynamic parameters \mathbf{M} and \mathbf{g} in a setting where

Data: $\mathcal{M}_i, \mathcal{G}_i, \mathbf{o}_{c_i}$
Input : $\mathbf{q}(t)$ the $(N \times 1)$ joints positions vector at time t
Output: The mass matrix \mathbf{M} and the gravity vector \mathbf{g}
Initialization;
 $\mathbf{M}, \mathbf{g}, \mathbf{J}_{c_i} = \mathbf{0}, {}^0\mathbf{T} = \mathbf{I}$
for $i \leftarrow 0$ **to** N **do**
 Step 1: Forward Kinematics
 ${}^{i-1}\mathbf{T} \leftarrow \theta_i;$
 ${}^0\mathbf{T} \leftarrow {}^0_{i-1}\mathbf{T} \cdot ({}^{i-1}\mathbf{T});$
 ${}^0\mathbf{o}_{c_i} \leftarrow {}^0_i\mathbf{T} \cdot ({}^i\mathbf{o}_{c_i});$
 Step 2: Computation of the Jacobian
 for $k \leftarrow 1$ **to** i **do**
 | $\mathbf{J}_{c_i}[1 \rightarrow 3][k] \leftarrow {}^0\mathbf{z}_k \times ({}^0\mathbf{o}_{c_i} - {}^0\mathbf{o}_k)$
 | $\mathbf{J}_{c_i}[4 \rightarrow 6][k] \leftarrow {}^0\mathbf{z}_k$
 Step 3: Computation of the Dynamic Parameters
 $\mathbf{M} \leftarrow \mathbf{M} + \mathbf{J}_{c_i}^T \mathcal{M}_i \mathbf{J}_{c_i};$
 $\mathbf{g} \leftarrow \mathbf{g} + \mathbf{J}_{c_i}^T \mathcal{G}_i;$

Algorithm 1: [Extended Structurally Recursive Algorithm (ESRA)]

the manipulator is not in contact with its environment. In the second set of experiments, external forces exerted on the end effector of the KUKA LBR IIWA are measured using a force/torque sensor to validate the the contact dynamic term $\mathbf{J}^T \mathbf{F}_{\text{ext}}$.

4.4.1 Validation by Simulation

The objective of these experiments is to validate the inertia matrix and gravity vector computations in a non-contact setting. To acquire the angular acceleration of the joints, the KUKA CAD model is imported into the Simscape Multibody™ simulation environment and a KUKA IIWA model is developed. This model relies on the inertia data provided by the CAD model. The Simscape software tool enables commanding joint torques or joint positions, and provides measurements of torque, position, velocity, and acceleration for each joint. A joint space trajectory (Figure 4.1) is generated and commanded to the actual robot, and joint torques (denoted Γ_{act}) are recorded at a sampling frequency 1 KHz

using the FRI library. The same trajectory is also applied to simulated robot and the joint acceleration and position data are recorded. These simulated joint trajectory data are utilized to calculate the joint torques Γ_{est} using equations (4.2) and (4.3). The proposed algorithm is validated by comparing Γ_{act} and Γ_{est} as illustrated in Figure 4.2. In addition, the joint torques computed by the Simscape model Γ_{sim} are also compared with Γ_{act} in Figure 4.3 for reference. The root mean square error is used to quantify the error between the measured and computed torque of a joint i . The results are shown in 4.1.

Table 4.1: Mean squared error of joint torques.

<i>Value</i>	J_1	J_2	J_3	J_4	J_5	J_6	J_7
<i>Sturs</i>	0.2013	1.1719	0.5927	1.0426	0.0719	0.1388	0.1052
<i>CAD</i>	0.4252	6.8725	2.1778	6.2711	0.2632	0.2465	0.0925

Figure 4.1: Joint space trajectory. The joints are actuated successively from first to seventh joint.

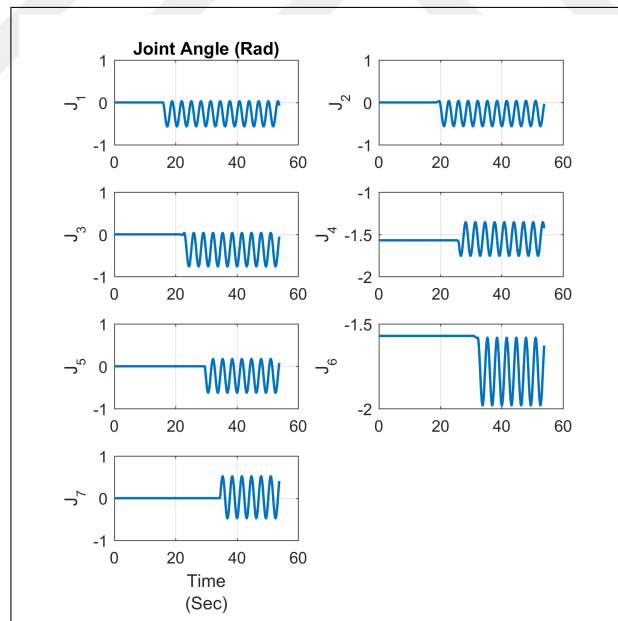


Figure 4.2: Model and actual torques using Sturs vales.

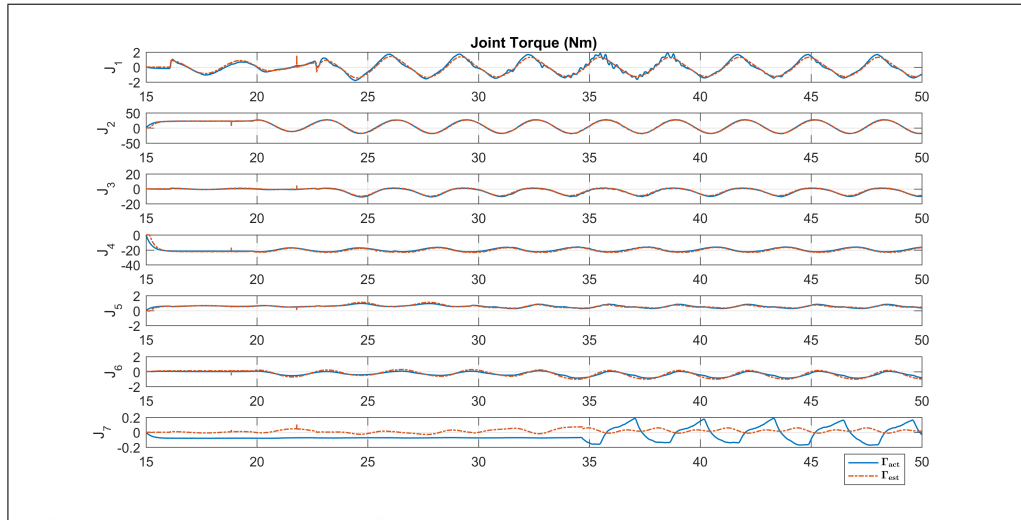
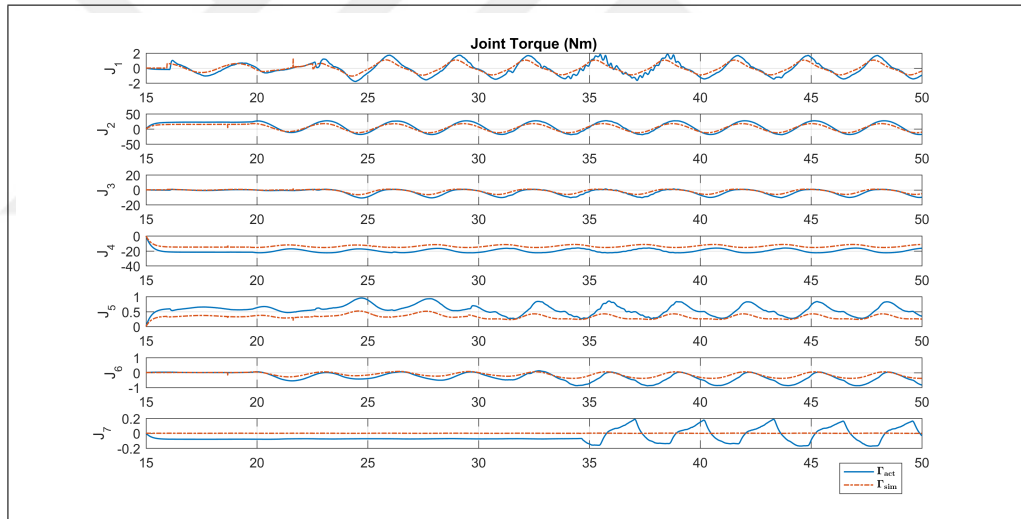


Figure 4.3: Model and actual torques using Cad vales.



4.4.2 Validation by Force/Torque Sensor

The total torque applied on each joint, can be measured by the torque sensors of the joints, this torque value contains all the dynamic terms (gravitational, inertial and external) torques, hence, after estimating the dynamic terms numerically using the suggested algorithm and by calculating the gravitational, inertial torques using the dynamic model,

one can estimate the external force by subtracting the measured torques from the model torques and multiply the resultant torque with the Jacobian transpose inverse. External forces and moments acting on the end-effector are compared with the real external forces and moments that are measured with a force/torque sensor mounted on top of the end effector (Figure 4.4). Results are illustrated in (Figure 4.5). The results shows nearly perfect match between the real and the estimated values, Except for n_z , duo to high frictional forces relative to gravitational forces.

Figure 4.4: Experiment setup.

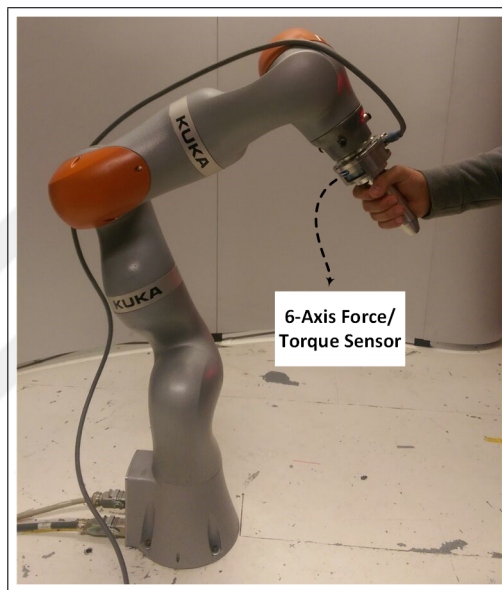
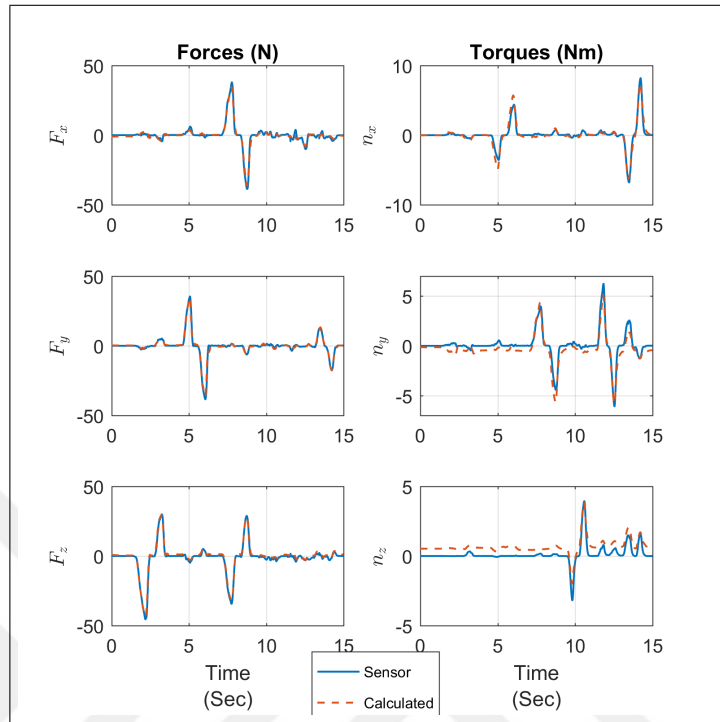


Figure 4.5: calculated End-effector Forces and torques validated with Force/torque sensor measurements.



5. TROCAR KINEMATICS

In robotic-assisted surgeries, the kinematics of the remote center of motion has always been a fundamental consideration for a variety of issues regarding the design, control, and optimization of Surgical robots. These issues arise due to the fact that the motion of the surgical instrument must yield to the constraint of the incision point (trocar) to ensure the safety of the incision. To tackle the control problem, many approaches are suggested in the literature. the proposed methods are mainly dynamic based (torque) or kinematic based (velocity or position).

Regarding Dynamic based control, Michelin et al. (2004b) proposed a control method that decouples the joint space torque into two components, task torque, and posture torque. Utilizing the null-space projection, the posture torque is computed such that it generates a zero force at the trocar. Aghakhani et al. (2013) derived a constraint jacobian $J_{RCM}(q, \lambda)$ which is dependent on the insertion rate λ and the joint positions q . then, they formulated the 'extended jacobian' which combines both jacobians (constraint and task space) and used it to design a velocity based controller. Starting from this constraint jacobian Sandoval et al. (2017) derived another constraint jacobian $J_{RCM}(q)$ that is independent of the insertion rate λ , through which torque control scheme became applicable. They applied torque control in two manners, where, in the first one, the commanded joint space torque vector is decomposed into sub-torque vectors each of which is responsible for a certain task identifiable by its jacobian. The primary task is set to maintain the RCM constraint then through the projection on the null space of the major task, the secondary task which is moving the surgical tool tip is performed. Their second method RCM and tool motion tasks are joined into one task which is given a top priority and other tasks are performed in the null space projection. However, these methods are not applicable in this system since direct torque control is not inherently supported by IIWA.

In the velocity approach, the main principle of control is to map the velocity of the tool trajectory to the joint space trajectory taking into account the trocar constraint (From,

2013)(Aghakhani et al., 2013)(Funda et al., 1996). However this method implies two issues. Firstly, the commands must be slow enough for the control loop to hold 2- that joint velocities must be observable (which is not the case in IIWA) in order to close a the control-loop. For this reason (Ortmaier & Hirzinger, 2000) developed a velocity observer in order to deploy their velocity based control approach on the 7-DoF AESOP ARM. On the other hand, Position control approach using the position kinematics seems to be a convection option. This method simply requires modeling the kinematics of the robotic structure taking into account the trocar constraint, then utilizing the model, forward and inverse kinematics (joint positions) are obtained and commanded to the robot (Michelin et al., 2004a) (Mayer et al., 2004). However, Michelin et al. (2004a) uses an optimization algorithm which is computationally less efficient and it is also less accurate than an explicit solution. Furthermore, (Michelin et al., 2004a) (Mayer et al., 2004) their methods do not provide singularity analysis.

5.1 VIRTUAL LAPAROSCOPIC ROBOTIC INSTRUMENT

The motion in manual laparoscopic surgeries is composed of three motion types:

- (a) A pivoting motion about the insertion point known as The remote center of motion(RCM).
- (b) Insertion.
- (c) Roll motion

1 and 2 can be modeled with virtual joints: two revolute and a prismatic joint (RRP) with mutually orthogonal axes intersecting at the insertion point. This structure provides translational motion with a spherical workspace that has a radius equal to the insertion depth provided by the prismatic joint. By adding a fourth revolute joint to represent the roll motion, the motion model of manual laparoscopy (also referred to as (4DOF RCM

Kuo & Dai (2012)) is fully covered by (RRPR) robotic structure as illustrated in Figure 5.1. Since this structure is inadequate to perform six degrees of freedom motion, a wrist mechanism with two orthogonal revolute joints can be integrated at the end of the insertion rod. This will result in a 'virtual' 6-DOF robot with (RRPRRR) structure. As such, given the desired wrist transformation, (RRR) orients the wrist whereas, (RRP) positions the insertion link accordingly. Thus, by defining a base frame centered at the trocar (Figure 5.2), a kinematic model of this virtual robot can be obtained using the Denavit-Hartenberg convention. As a result, forward, inverse and velocity kinematics can be obtained using the traditional formulations.

In this study, the degrees of freedom that are responsible for the manual laparoscopic motion (RRPR) are referred to as ψ , ϕ , ρ and γ , respectively. The motion of these virtual joints is provided by the robotic manipulator IIWA after performing the necessary mapping. While α and β are real joints, their motion is provided by the integrated robotic wrist. Figure 5.2 depicts the concept of the proposed Virtual Laparoscopic Robotic Instrument model.

Figure 5.1: RRPR Model of the manual laprascopic motion.

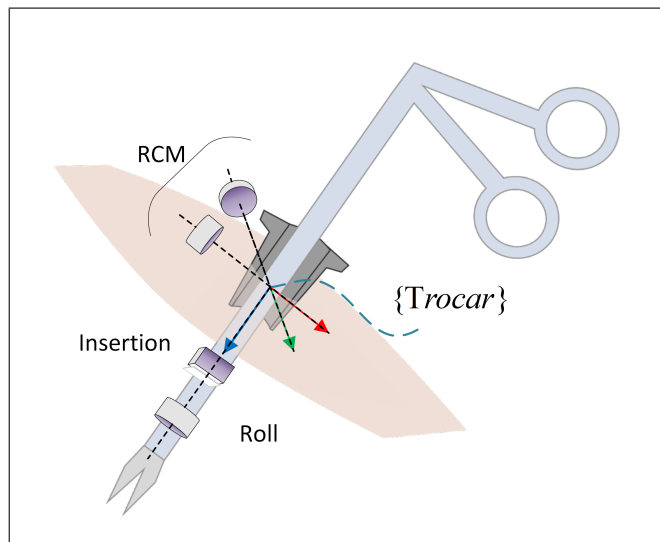


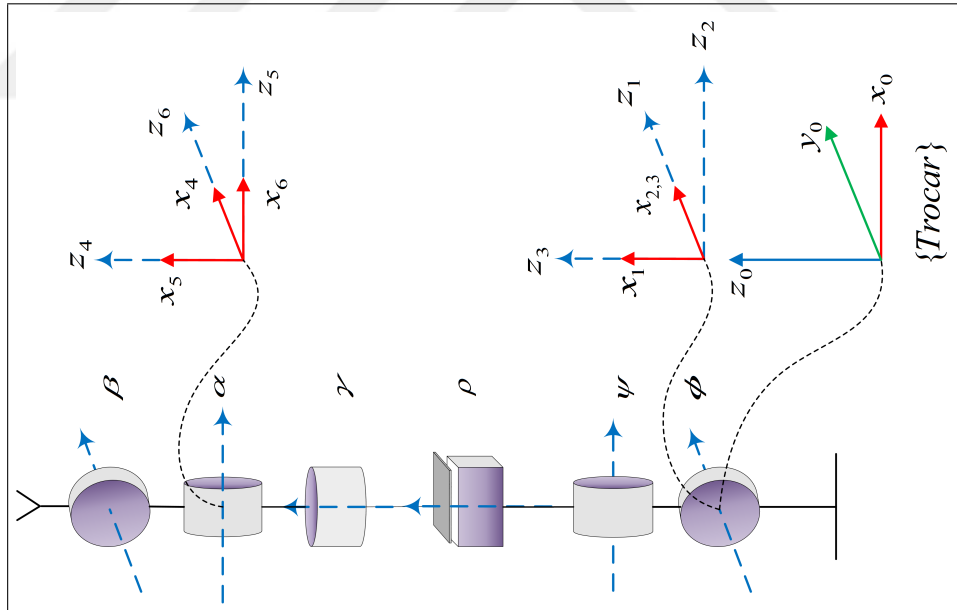
Table 5.1: DH parameters of the Virtual Laparoscopic Robotic Instrument

Joint	a_{i-1}	α_{i-1}	d_i	θ_i
1	0	$-\pi/2$	0	$-\pi/2 + \phi$
2	0	$-\pi/2$	0	$-\pi/2 + \psi$
3	0	$-\pi/2$	ρ	0
4	0	0	0	γ
5	0	$\pi/2$	0	$\pi/2 + \alpha$
6	0	$\pi/2$	0	$\pi/2 + \beta$

5.2 FORWARD KINEMATICS

It is essential to perform forward kinematic analysis to obtain symbolic representations of link transformations that will later be used to obtain the inverse kinematics. Frame assignment Figure 5.2 and the DH parameters in table 5.1 are obtained using the modified convention. Also, link transformations are obtained through:

Figure 5.2: Frame assignment of the Virtual Laparoscopic Robotic Instrument using the modified convention.



$${}_{i-1}^i\mathbf{T} = \begin{bmatrix} c\theta_i & -s\theta_i & 0 & a_{i-1} \\ s\theta_i c\alpha_{i-1} & c\theta_i c\alpha_{i-1} & -s\alpha_{i-1} & -s\alpha_{i-1}d_i \\ s\theta_i s\alpha_{i-1} & c\theta_i s\alpha_{i-1} & c\alpha_{i-1} & c\alpha_{i-1}d_i \\ 0 & 0 & 0 & 1 \end{bmatrix} \quad (5.1)$$

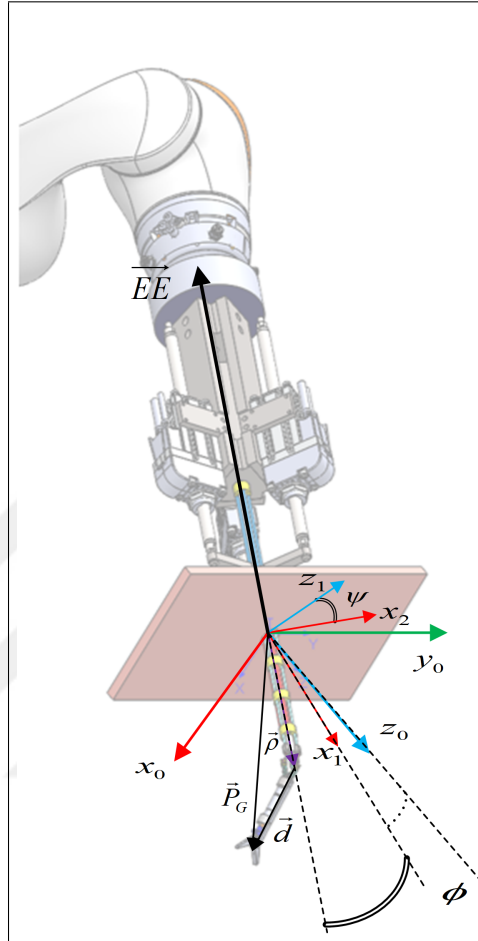
5.3 INVERSE KINEMATICS

The derivation of the inverse kinematic equations are publishes and well explained in (Alassi et al., 2018) Therefore in this section only the final results are shown.

With reference to figure 5.3 and knowing that 0_GT is the reference transformation matrix in Eq.5.2

$${}^0_GT = \left[\begin{array}{ccc|c} R_G & & & P_G \\ \hline 0 & 0 & 0 & 1 \end{array} \right] \quad (5.2)$$

Figure 5.3: Visualization of the RCM joints ϕ, ψ and ρ in addition to \vec{P}_G and \vec{d} vectors.



The joint values of the Virtual Robotic Instruments are:

$$\vec{\rho} = \vec{P}_G - \vec{d} \quad (5.3)$$

$$\phi = \text{atan2}({}^0\rho_x, {}^0\rho_z) \quad (5.4)$$

$$\psi = \text{atan2}(-{}^1\rho_z, {}^1\rho_x) \quad (5.5)$$

$${}^3\mathbf{R}_G = ({}^0_3\mathbf{R}^{-1})\mathbf{R}_G \quad (5.6)$$

Considering the numeric values of ${}^3_6\mathbf{R}$ to be r_{ij} , the solution yields to:

$$\alpha = \text{asin}(r_{33}) \quad (5.7)$$

$$\beta = \text{atan2}(-r_{31}, -r_{32}) \quad (5.8)$$

$$\gamma = \text{atan2}(r_{23}, r_{13}) \quad (5.9)$$

where $-90^\circ < \beta < 90^\circ$, $-175^\circ \leq \gamma \leq 175^\circ$ and $-90^\circ < \alpha < 90^\circ$.

Notice that for systems that use a prismatic joint to feed the insertion (*i.e.*, da Vinci), ρ can directly be provided by that prismatic joint's motion. Whereas for systems that use the Cartesian motion of the end effector to drive the insertion (*i.e.*, DLR MIRO) and the system presented in this paper, further computations are necessary. In order to map ${}^0\vec{\rho}$ to the end effector position ${}^0\overrightarrow{EE}$, the unit vector of ${}^0\vec{\rho}$ can first be defined in the form of

$$\vec{u} = \frac{{}^0\vec{\rho}}{\|{}^0\vec{\rho}\|} \quad (5.10)$$

Since ${}^0\vec{\rho}$ and ${}^0\overrightarrow{EE}$ are collinear, and noticing that their directions are opposite, ${}^0\overrightarrow{EE}$ can be calculated with the following formula:

$${}^0\overrightarrow{EE} = -(L - \rho)\vec{u} \quad (5.11)$$

where L is the total length between the end effector the wrist center Figure ???. Also, notice that for any driving mechanism, maintaining the RCM constrain requires the orientation

of the end effector to have the same orientation of frame $\{4\}$, thus:

$${}^0_{EE}\mathbf{R} = {}^0_4\mathbf{R} \quad (5.12)$$

since the position and the orientation of the end effector are determined by Eq. 5.11 and 5.12, we can control the robot in joint space position control mode by solving the manipulator's inverse kinematics.

5.4 JACOBIAN AND SINGULARITY ANALYSIS

The Jacobian is a matrix that maps joint space to task space velocities. This mapping is expressed in the form of ?:

$$\dot{\mathcal{V}} = \mathbf{J}\dot{q} \quad (5.13)$$

where $\dot{\mathcal{V}}$ is a vector of task space velocities expressed in the Jacobian frame, and \dot{q} is the joint space velocity vector. Using equation 5.13 the velocity of the wrist tool frame described in the trocar frame can be obtained. A symbolic form of the Jacobian can be obtained using Robotica package provided by Nethery & Spong (1994) with taking into account necessary modifications to comply with the modified convention. Eq. 5.14 shows Jacobian matrix of the Virtual Laparoscopic Robotic Instrument where the notations of c and s symbolize *cosine* and *sine* functions, respectively.

$$J = \begin{pmatrix} \rho c_\phi c_\psi & -\rho s_\phi s_\psi & c_\psi s_\phi & 0 & 0 & 0 \\ 0 & -\rho c_\psi c_\phi^2 - \rho c_\psi s_\phi^2 & -s_\psi & 0 & 0 & 0 \\ -\rho c_\psi s_\phi & -\rho c_\phi s_\psi & c_\phi c_\psi & 0 & 0 & 0 \\ 0 & c_\phi & 0 & c_\psi s_\phi & c_\phi c_\gamma + s_\phi s_\psi s_\gamma & c_\gamma c_\alpha s_\phi s_\psi - c_\phi c_\alpha s_\gamma + c_\psi s_\phi s_\alpha \\ 1 & 0 & 0 & -s_\psi & c_\psi s_\gamma & c_\psi c_\gamma c_\alpha - s_\psi s_\alpha \\ 0 & -s_\phi & 0 & c_\phi c_\psi & c_\phi s_\psi s_\gamma - c_\gamma s_\phi & c_\alpha s_\phi s_\gamma + c_\phi (c_\gamma c_\alpha s_\psi + c_\psi s_\alpha) \end{pmatrix} \quad (5.14)$$

Singularities can be obtained as well when the determinant of the Jacobian is zero :

$$Det(\mathbf{J}) = -\rho^2 c_\psi c_\alpha \quad (5.15)$$

Thus, 5.15 is zero when

$$\begin{aligned}\rho &= 0 \\ \psi &= \pm\pi/2 \\ \alpha &= \pm\pi/2\end{aligned}\tag{5.16}$$

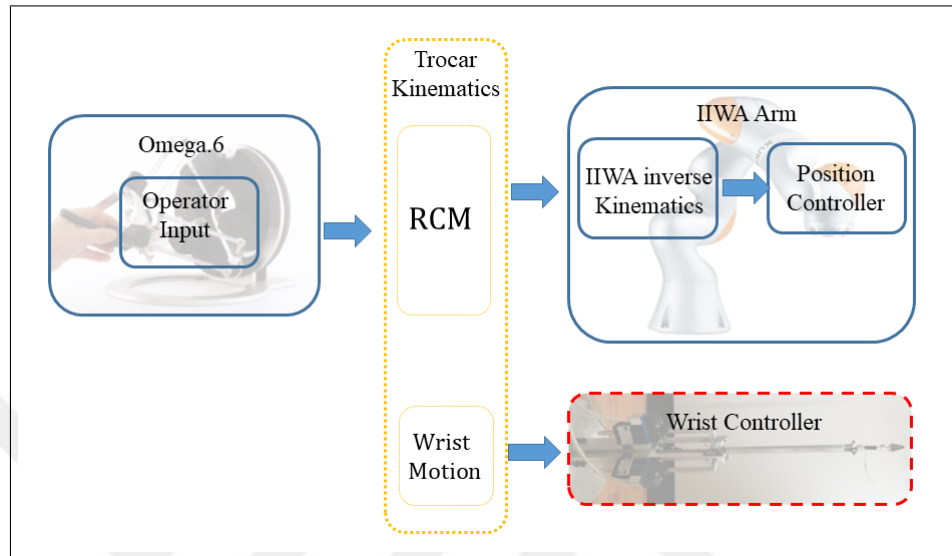
These singularities agree with inverse kinematics solution. Indeed, as α approaches 90 degrees, γ and β changes instantaneously from $\pi/2$ to $-\pi/2$ or vice versa, since the denominator of equations 5.8 and 5.9 contains $\cos\alpha$. The same discussion is valid for ψ , when the denominator of equation 5.4 is zero. The most serious case happens when ρ is near zero, small motion of the wrist tool requires a very large motion for the driving manipulator. Also, notice, when $\rho = 0$ the robot loses two operational space degrees of freedom, since moving the insertion rod on x and y will no longer be possible.

Recognizing these singularities is significant for systems that use artificially constrained RCM because the controller might fail to maintain the constraint.

5.5 POSITION CONTROL

Since, the kinematic solution is available, the combined Wrist-Manipulator structure can be controlled in position mode as illustrated in figure 5.4. It should be pointed out that the control signal of joint angles is filtered using a low pass filter with a cutoff frequency of 1 Hz. This filtering is important to protect the manipulator from high-frequency commands that cause high inertial loads on joint motors.

Figure 5.4: The control block diagram of the combined Wrist-Manipulator structure. Blocks that are red framed with a dashed line represents work conducted by (Bazman et al., 2018). Blocks that are orange framed with a dotted line represents joint work documented in (Alassi et al., 2018). Blocks framed otherwise are thesis work.



6. SIMULATION

6.1 INTRODUCTION

So far, we have solved the kinematics problem for of the combined IIWA-wrist structure. Yet to examine the solution and to manipulate the surgical tool in real time we need to integrate the 6-DOF haptic device Omega.6. As such we will not only be able to command transformation but also to get a stream of the contact force which is exerted on the surgical tool.

6.2 MATLAM-SIMULINK SIMULATION ENVIRONMENT

As Omega.6 uses C++ to communicate with the computer, the so-called s-Function can be used to interface the device to Simulink. S-Functions are dynamically linked subroutines MATLAB execution engine can automatically load and execute. As such, the position and orientation data can be acquired from the device, and the force of contact can be feedback to the device. However, to simulate force contact we need to model a contact environment or a “virtual wall”. This was done using hooks law:

$$F = k\Delta x \quad (6.1)$$

where F is the reaction force acting on the tip of the surgical forceps. K is the modulus of elasticity and Δx is the penetration depth.

Figure 6.1 illustrates Omega’s interface to Simulink along with the virtual wall. Figure 6.2 depicts forces of interaction with the virtual wall. Finally, figure 6.3 shows the system in action for various configuration commanded to the system through Omega.6 by the user.

Figure 6.1: Omega.6 interface to Simulink implemented using inlined C++ S-Function.

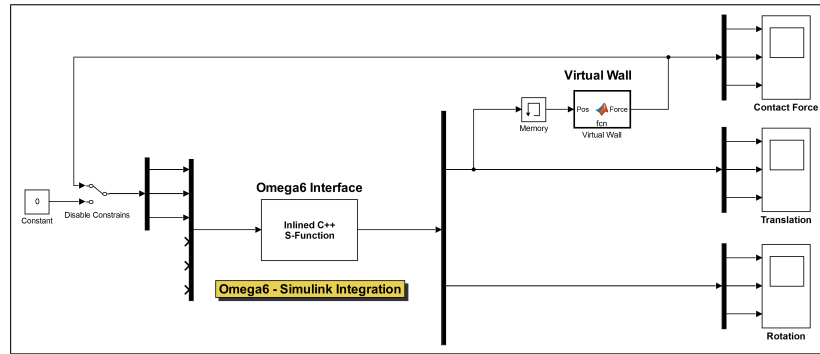


Figure 6.2: The Contact force with their corresponding to virtual walls. Forces are generated whenever the position is less than zero along the three dimensions.

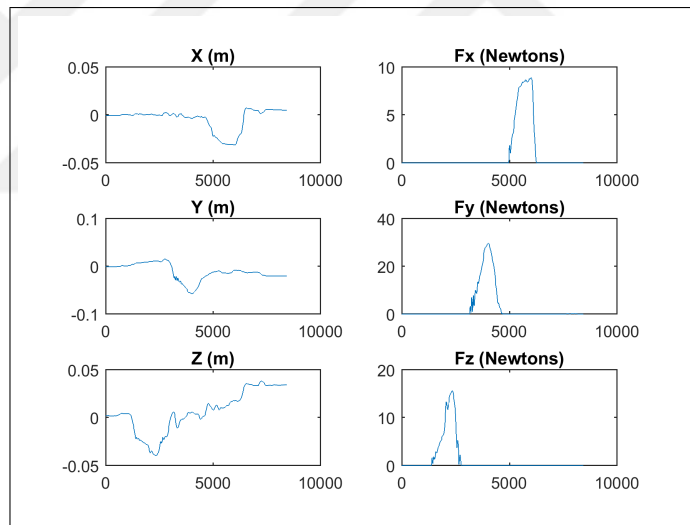
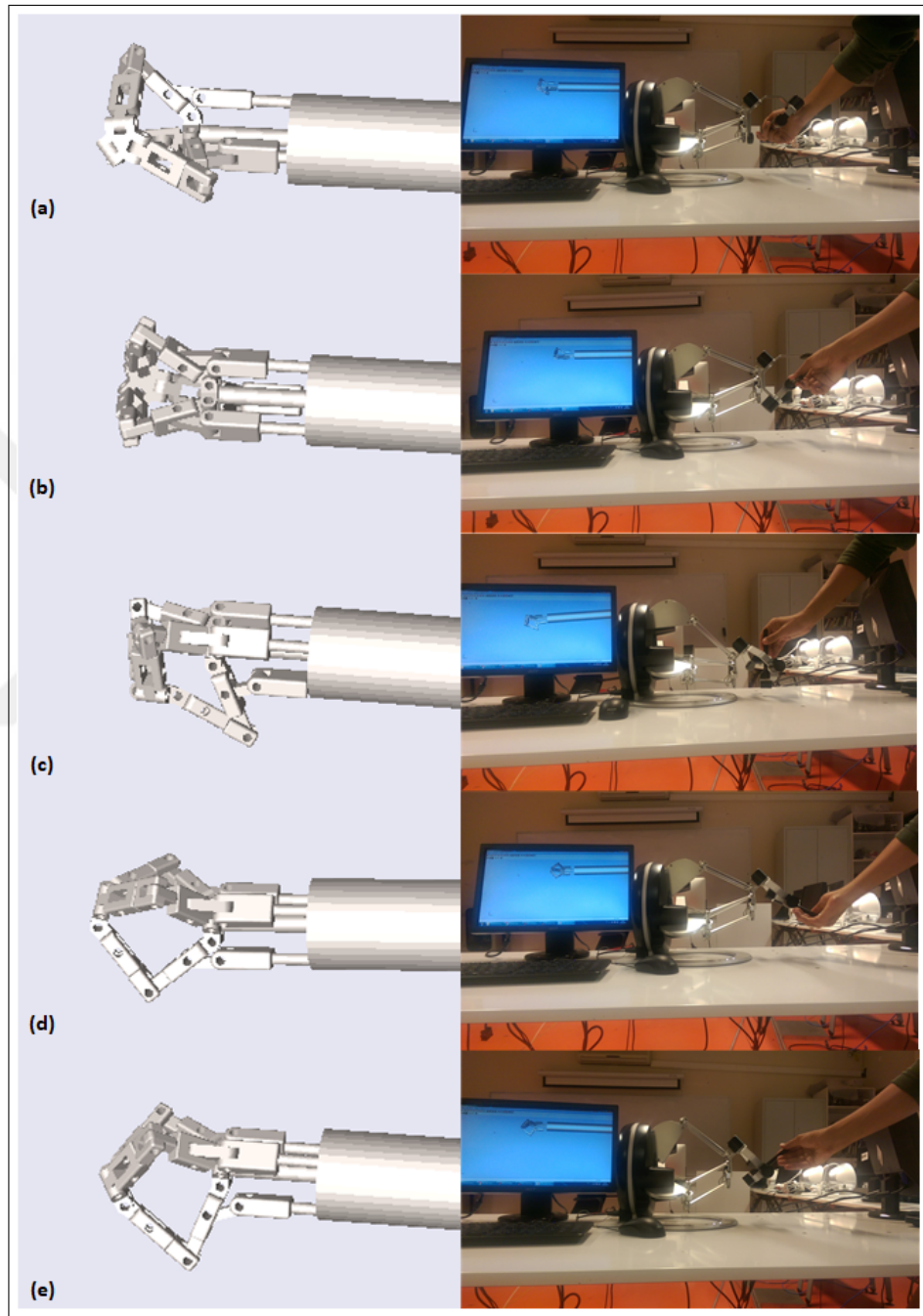


Figure 6.3: Pitch, Yaw and Roll control through the integrated haptic device. The commanded values are: a) and b) yaw near 90 and -90 respectively, c) and d) Pitch near 45 and -70 respectively and e) is the initial orientation where roll, pitch, and yaw are zeros.



7. SYSTEM ARCHITECTURE AND IMPLEMENTATION

7.1 SYSTEM COMPONENTS

7.1.1 Omega.6

Omega.6 is a parallel robotic mechanism with a 3-R type wrist mounted on top of it. The parallel mechanism is actuated with tendon-driven joints to provide both the Cartesian translational motion in addition to translational haptic feedback. On the other hand, the wrist is merely a serial chain of three encoders that are not actively actuated hence, it only captures the commanded orientation. The Haptic SDK and Robotic SDK are two C++ based libraries that represent the software interface of the device. Whereas the physical interface of the device is USB.

7.1.2 The Kuka IIWA 7 R800 Robot

The redundant Kuka IIWA manipulator is used to provide the remote center of motion (RCM) to locate the wrist mechanism as desired. The robot controller is set to joint position control mode. The joint space trajectory can be commanded via the built-in UDP based interface: FRI (Fast Robot Interface). This FRI library is implemented in C++.

7.1.3 The Wrist Mechanism

The wrist mechanism is a parallel robotic structure developed by (Bazman et al., 2018) that has the ability to move the attached gripper in 3 Degrees of freedom (Pitch, Yaw, and radial linear motion) in addition to the gripping degree of freedom. The wrist is actuated through three DC type linear motors. The motion is transferred from the motors to the wrist joints through rigid rods, this makes the wrist superior to its counterpart tendon-

driven wrist since these kinds of wrists are poorly back-drivable. The back drivability of the wrist is a key attribute because it allows for a feasible force estimation by using a disturbance observer (Yilmaz et al., 2018).

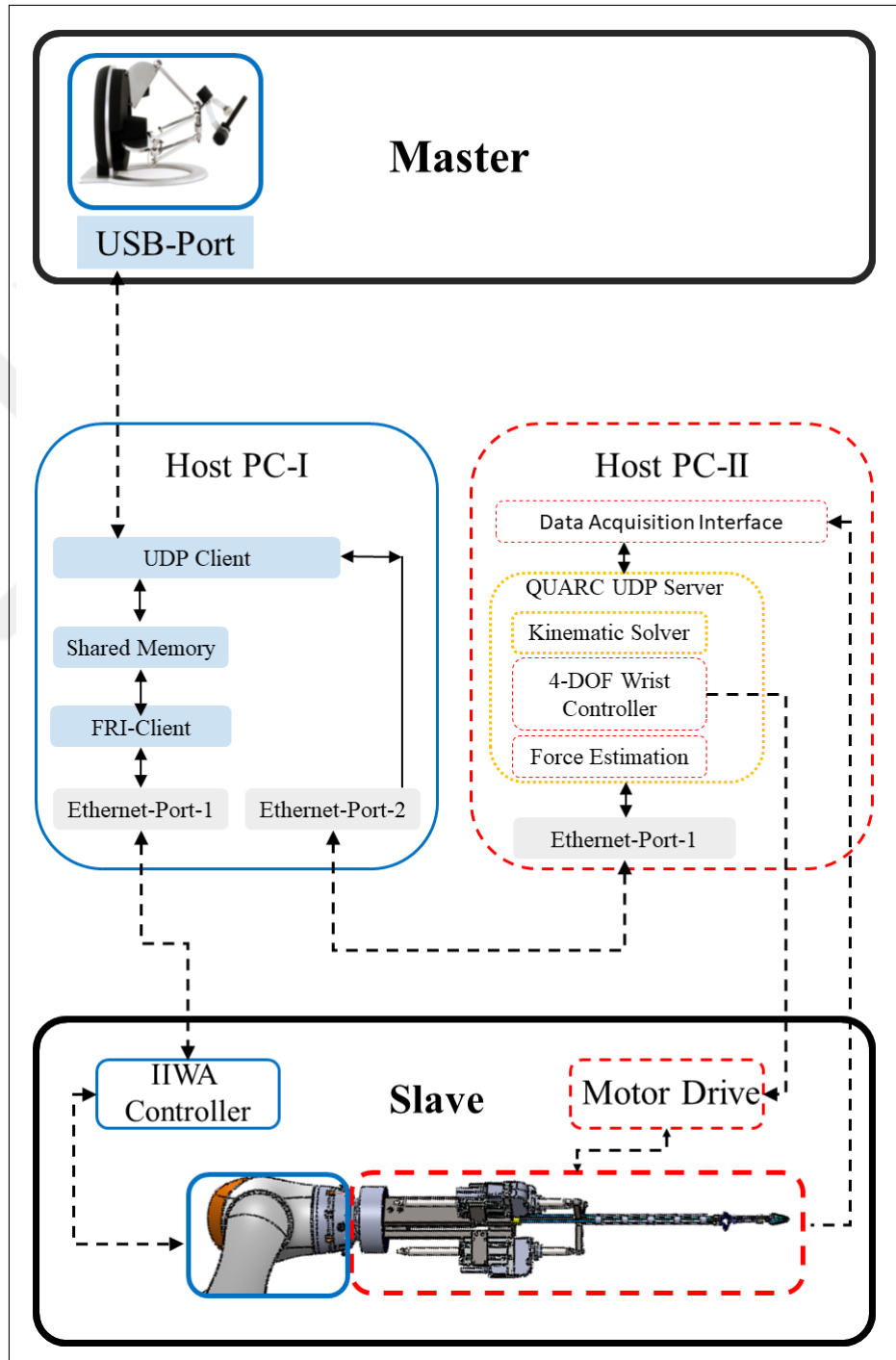
7.2 SYSTEM INTEGRATION

The wrist mechanism and the commercial Kuka IIWA robot are integrated as depicted in Fig. 7.1. The architecture is based on multiprocessing and networking. Multiprocessing is handled by the first host computer (PC-1) which is running two major processes:

- The interface to IIWA controller (FRI client). This process handles the communication with IIWA controller.
- A UDP based client node. This process handles the communication between the haptic device (Omega.6) and PC-1 in one side, and the communication between PC-1 and the second host computer (PC-2) on the other side.

These two processes exchange data through a shared memory segment allocated by the operating system. Hence, other processes such as (a process handling and processing a camera stream) can be integrated into the system through accessing the shared memory segment. As such extensibility is guaranteed. After Omega.6 commands and IIWA state are acquired, they are sent through the UDP client node to the server node hosted by PC-2. The server node is running on Quarc which is a real-time operating system that uses Windows to execute controller routine. Also, this node is responsible for: computing the inverse kinematics, controlling the wrist, as well as running the external force estimator.

Figure 7.1: A functional diagram representing the distributed control scheme of the proposed surgical robotic platform. Blocks that are red framed with a dashed line represents work conducted by (Bazman et al., 2018) and (Yilmaz et al., 2018). Blocks that are orange framed with a dotted line represents joint work documented in (Alassi et al., 2018). Blocks framed otherwise are thesis work



7.3 DATA FLOW AND SIGNAL TRANSFER

Data flow starts from host device H-1 where the command is acquired from the haptic device Omega.6 and sends it together with IIWA arm joint state (position, Torque) through the UDP-Client node to the Quarc side in Host device H-2. Meanwhile, the UDP-Client loop blocks until the inverse kinematic solution is solved together with estimated forces from Quarc server back to the UDP-Client node. This blocking in the UDP-Client node should provide synchronization between the two routines running on H-1 and H-2. Figure 7.2 illustrates data flow architecture. To facilitate data transmission, the transmitted values are converted from Double-precision floating-point format to string format. The pressure conversion and transmission is explained in figure 7.3

Figure 7.2: A flow chart representing the communication logic.

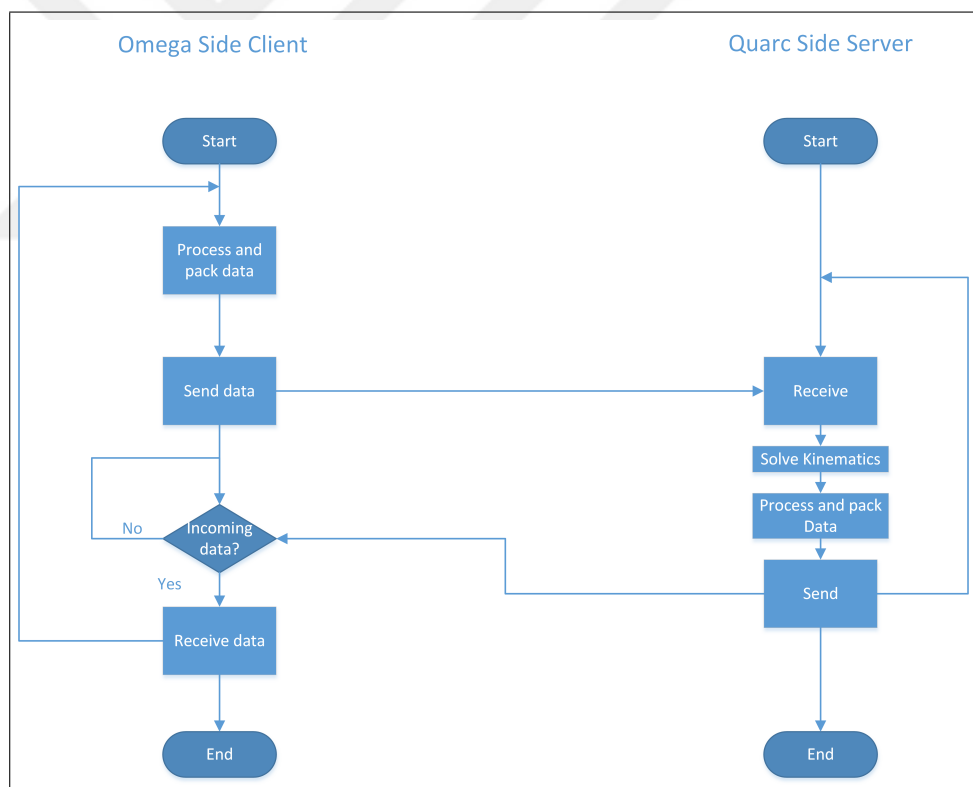
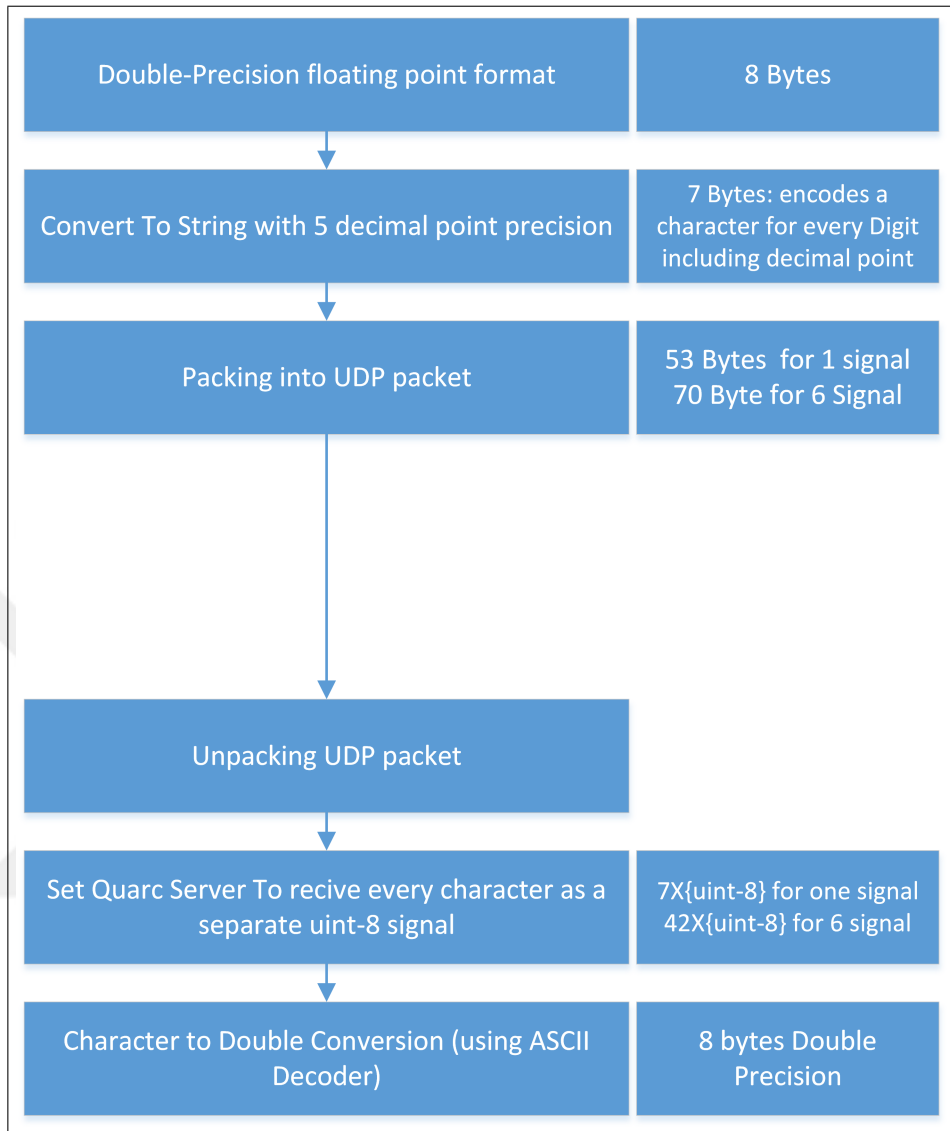


Figure 7.3: Signal Packing.



8. EXPERIMENTS AND RESULTS

8.1 VALIDATION OF ROTATIONAL MOTION

The objective of this experiment is to assess the performance of the system when executing pure rotational commands: pitch, yaw, and roll. Since the translational commands are fixed, consequently, the system must maintain the commanded position while the orientation is changing. Using the haptic device, the operator commands the angular trajectory while the translational trajectory is fixed at (0,0,160) mm on x,y, and z, respectively w.r.t trocar. The executed joint space trajectory is recorded for 71.9 sec with 1 kHz sampling frequency and used to reproduce the link transformations which are used to reproduce the posture of the virtual robot. Fig. 8.1. To quantify the ability of the system to maintain the commanded position, the mean and standard deviation of the executed position trajectory are calculated. Ideally, the mean of the executed trajectory should be equal to the commanded position. Any bias from the mean represents a systematic positioning error. This error is caused by the accuracy of the encoders as well as the steady-state error of both IIWA and the wrist controllers. The results presented in Table 8.1 indicates a good accuracy of less than 0.6 mm on three the axes. On the other hand, the small standard deviation indicates an acceptable precision with less than 2 mm. This random error is mostly due to differences in the dynamic response for the two robots causing asynchronous motion between ψ , ϕ , γ , and ρ in one side and α and β in the other.

Table 8.1: Statistical values of the rotational motion experiment. The values are measured in millimeters.

<i>Value</i>	<i>x</i>	<i>y</i>	<i>z</i>
μ	-0.0703	0.2504	160.4918
σ	1.0695	1.1668	0.4493
max	2.8709	3.6636	161.8600
min	-4.0522	-2.1340	159.4403

Figure 8.1: (a) Posture plot of the Virtual Laparoscopic Robotic Instrument for randomly showing the gripper (magenta) and its frame while approaching a target point from different directions. The insertion link (black) performing RCM motion .Where (a) is a 3D perspective and (b) depicts the view from X-Y axis

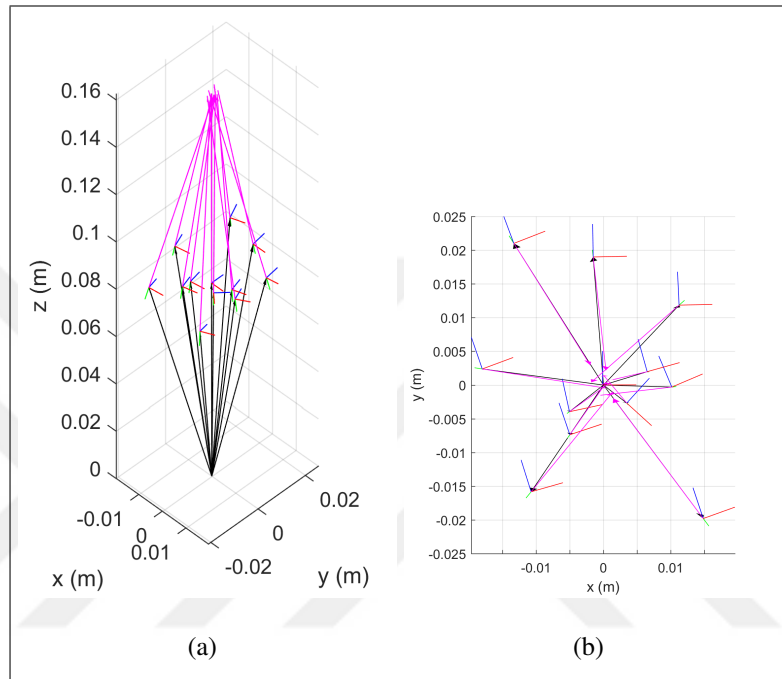


Figure 8.2: Rotational Experiment Data.

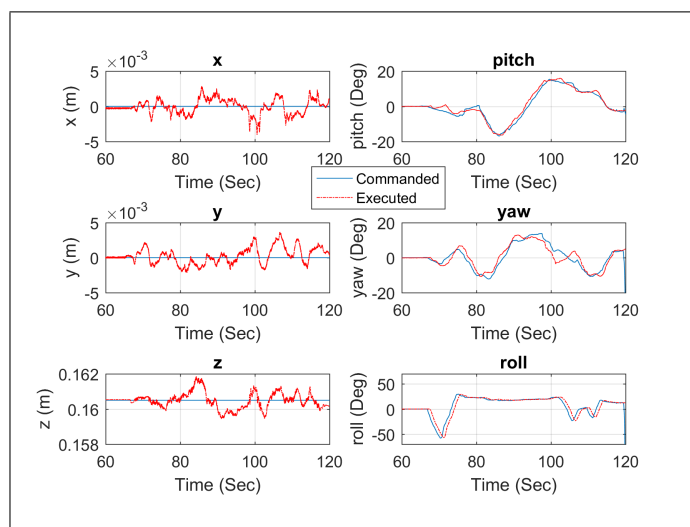
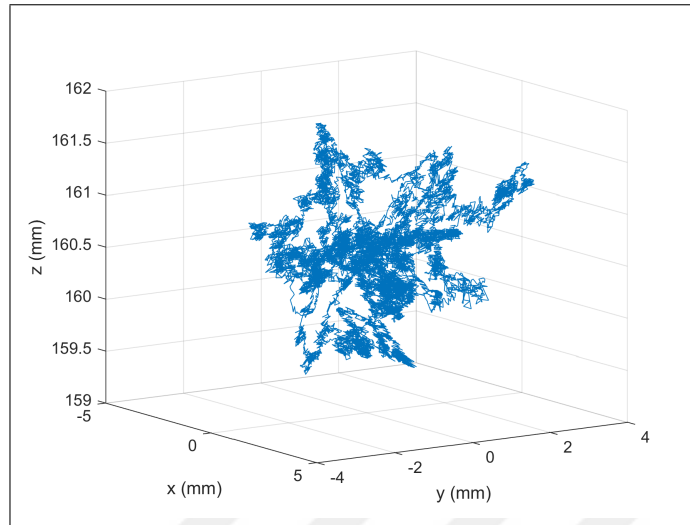


Figure 8.3: The Random translational motion of the gripper.



8.2 BILATERAL TELEOPERATION EXPERIMENTS

Multiple experiments are conducted to illustrate the ability of the system to measure external forces and torques of IIWA-Forceps System. Position-Force bilateral teleoperation is performed for each motion axis of the laparoscopic motion. We will illustrate in each subsection the procedure through which each force/torque value is measured.

NOTE: Frame axis x , y , and z are identified with the colors: red, green and blue respectively.

Since it is difficult to design an experiment to observe torque resulting from rotational interaction with the environment, we used a different approach. In this experiment, a human manually twists the forceps about its z (this motion is represented by angular velocity vector in figure 10) and since the IIWA is operated in impedance control mode, the robot will react with a torque opposing the applied motion according to Hook's law. Since Omega haptic device lacks the ability to reflect torques, this torque is observed in figure 8.7.

Figure 8.4: Bilateral teleoperation experiments.

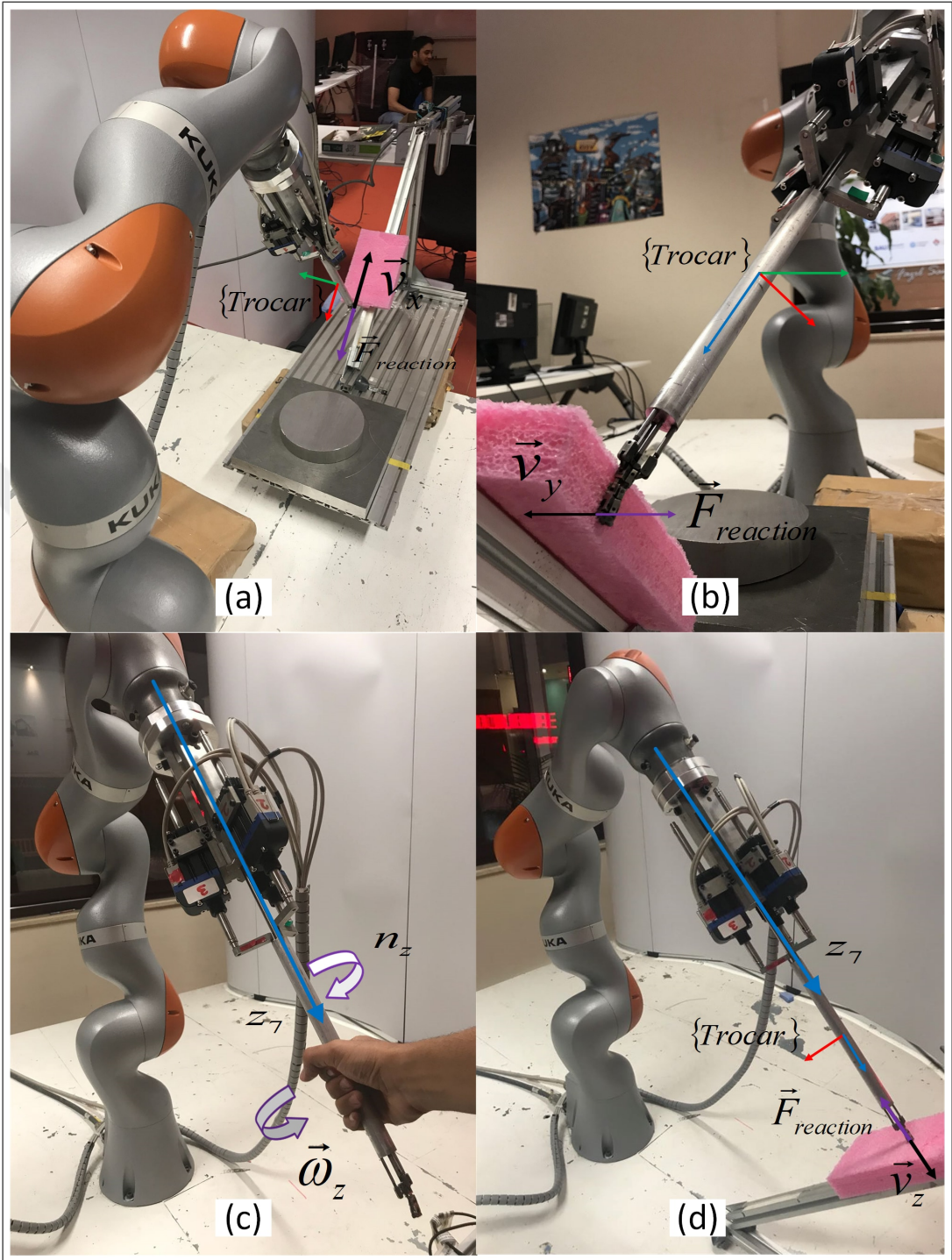


Figure 8.5: Experiment results for x-axis.
(a) Shows the position of the TCP and the object's edge, a contact occurs each time the TCP crosses object edge towards the negative x. (b) Depicts the reaction force that is reflected to the master side.

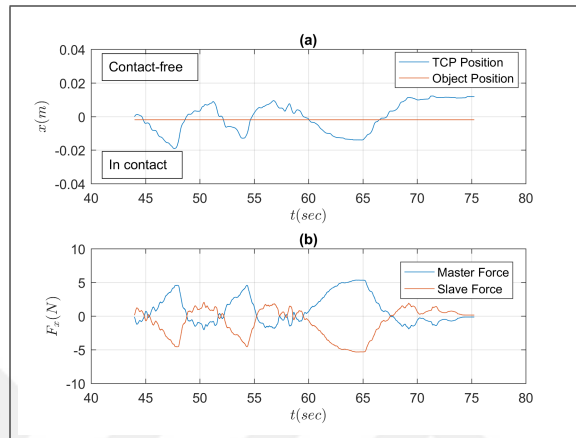


Figure 8.6: Experiment results for y-axis.
(a) Shows the position of the TCP and the object's edge, a contact occurs each time the TCP crosses object position towards the negative y. (b) Depicts the reaction force that is reflected to the master side.

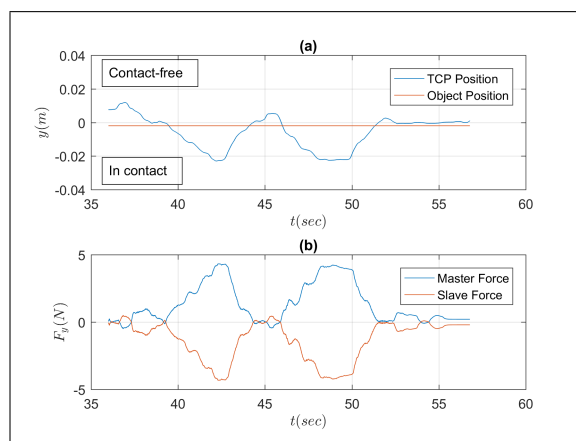
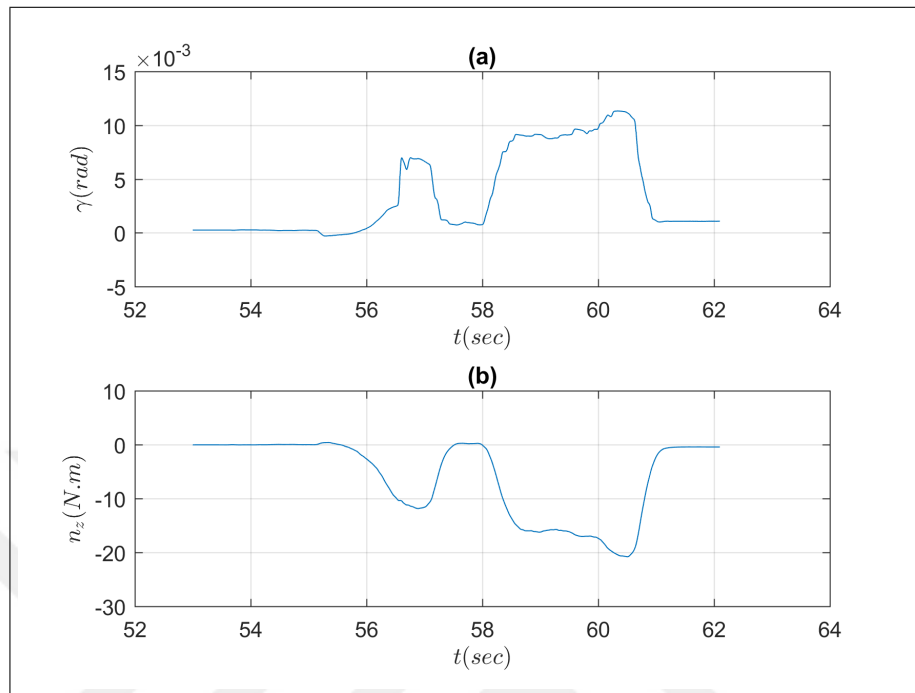


Figure 8.7: Experiment results for z-axis. (a) Shows the Euler angle γ . (b) Depicts the robot torque that is induced by the robot according to Hooke's law



9. CONCLUSIONS

In this thesis, a redundant manipulator is integrated to a platform for robotic-assisted laparoscopic surgeries. The platform consists of an in-house designed wrist mechanism mounted on the serial manipulator KUKA IIWA to form a total of 10+1 DoF hyper-redundant robotic structure. The redundancy of the RCM manipulator is utilized to avoid joint limits during real-time teleoperation. Also, using the concept of 'Virtual Laparoscopic robotic instrument' it was possible to solve the inverse kinematics of the combined robotic structure with respect to the trocar point. This solution is used to control the surgical platform in position control mode. On the hardware level, a modular architecture is proposed to integrate the haptic device into the system such that real-time bilateral teleoperation became feasible in addition to performing dynamic analysis to the utilized manipulator for the same purpose. Also, a Human-in-the-loop simulation environment is developed for the system. This platform facilitates the testing procedure for the kinematic controller and provides a safety layer In the sense that the operator is trained on simulation before applying it on the real platform.

Unilateral and bilateral telemanipulation scenarios are designed and applied on the real platform to validate the system. The system illustrated a good overall performance with acceptable accuracy. To summarize :

- (a) A closed form 7-DoFs analytic Inverse kinematic solution of KUKA IIWA is Obtained.
- (b) A redundancy resolution that avoids joint limits in real time is Proposed. Two algorithms are developed to implement the proposed resolution. Both algorithms succeeded to avoid joint limit during teleoperation.
- (c) Developed an efficient algorithm to obtain the Kuka IIWA dynamic terms: the mass matrix and the gravity vector.

- (d) A simulation environment is developed.
- (e) An integration architecture for real-time control of the surgical robotic system is proposed and implemented.
- (f) The surgical robotic platform is tested through multiple experiments. The system illustrated a good performance with a maximum error of 3.66 mm in position control mode.



REFERENCES

Books

Craig, J., 2005. *Introduction to Robotics: Mechanics and Control*. Addison-Wesley series in electrical and computer engineering: control engineering. Pearson/Prentice Hall.

W., S. M., Seth, H., & Vidyasagar, M., 2004. *Robot Dynamics and Control* , pp. 155–210.



Periodicals

- Aghakhani, N., Geravand, M., Shahriari, N., Vendittelli, M., & Oriolo, G., 2013. Task control with remote center of motion constraint for minimally invasive robotic surgery. In *Robotics and Automation (ICRA), 2013 IEEE International Conference on*. IEEE, pp. 5807–5812.
- Aksungur, S., 2015. Remote center of motion (rcm) mechanisms for surgical operations. *International Journal of Applied Mathematics, Electronics and Computers* **3(2)**, pp. 119–126.
- Alassi, A., Yilmaz, N., Bazman, M., Gur, B., & Tumerdem, U., 2018. Development and kinematic analysis of a redundant, modular and backdrivable laparoscopic surgery robot. In *Proceedings of the International Conference on Advanced Intelligent Mechatronics (AIM)*. p. 1.
- Bazman, M., Yilmaz, N., & Tumerdem, U., 2018. Dexterous and back-drivable parallel robotic forceps wrist for robotic surgery. In *2018 IEEE 15th International Workshop on Advanced Motion Control (AMC)*. pp. 153–159.
- Brisson, G., 2017. Tele-operative surgical systems and methods of control at joint limits using inverse kinematics. US Patent App. 15/126,967.
- De Groen, P. C., 2017. History of the endoscope [scanning our past]. *Proceedings of the IEEE* **105(10)**, pp. 1987–1995.
- Faria, C., Ferreira, F., Erhagen, W., Monteiro, S., & Bicho, E., 2018. Position-based kinematics for 7-dof serial manipulators with global configuration control, joint limit and singularity avoidance. *Mechanism and Machine Theory* **121**, pp. 317–334.
- Featherstone, R., 1983. The calculation of robot dynamics using articulated-body inertias. *The International Journal of Robotics Research* **2(1)**, pp. 13–30.
- Featherstone, R. & Orin, D., 2000. Robot dynamics: equations and algorithms. In *Proceedings 2000 ICRA. Millennium Conference. IEEE International Conference on Robotics and Automation. Symposia Proceedings (Cat. No.00CH37065)*, vol. 1. pp. 826–834 vol.1.
- Food and Drug Administration, 2017. Clearance report. https://www.accessdata.fda.gov/cdrh_docs/pdf17/K171120.pdf. [Online; accessed 27-April-2018].
- From, P. J., 2013. On the kinematics of robotic-assisted minimally invasive surgery. *Modeling, Identification and Control* **34(2)**, p. 69.
- Funda, J., Taylor, R. H., Eldridge, B., Gomory, S., & Gruben, K. G., 1996. Constrained cartesian motion control for teleoperated surgical robots. *IEEE Transactions on Robotics and Automation* **12(3)**, pp. 453–465.

- Gallagher, A., McClure, N., McGuigan, J., Ritchie, K., & Sheehy, N., 1998. An ergonomic analysis of the fulcrum effect in the acquisition of endoscopic skills. *Endoscopy* **30(07)**, pp. 617–620.
- Gaz, C., Flacco, F., & Luca, A. D., 2014. Identifying the dynamic model used by the kuka lwr: A reverse engineering approach. In *2014 IEEE International Conference on Robotics and Automation (ICRA)*. pp. 1386–1392.
- Gidaro, S., Buscarini, M., Ruiz, E., Stark, M., & Labruzzo, A., 2012. Telelap alf-x: a novel telesurgical system for the 21st century. *Surgical technology international* **22**, pp. 20–25.
- Hagn, U., Nickl, M., Jörg, S., Passig, G., Bahls, T., Nothhelfer, A., Hacker, F., Le-Tien, L., Albu-Schäffer, A., Konietschke, R. et al., 2008a. The dlr miro: a versatile lightweight robot for surgical applications. *Industrial Robot: An International Journal* **35(4)**, pp. 324–336.
- Hannaford, B., Rosen, J., Friedman, D. W., King, H., Roan, P., Cheng, L., Glozman, D., Ma, J., Kosari, S. N., & White, L., 2013. Raven-ii: an open platform for surgical robotics research. *IEEE Transactions on Biomedical Engineering* **60(4)**, pp. 954–959.
- Kalan, S., Chauhan, S., Coelho, R. F., Orvieto, M. A., Camacho, I. R., Palmer, K. J., & Patel, V. R., 2010. History of robotic surgery. *Journal of Robotic Surgery* **4(3)**, pp. 141–147.
- Khatamian, A., 2015. Solving kinematics problems of a 6-dof robot manipulator. In *Proceedings of the International Conference on Scientific Computing (CSC)*. The Steering Committee of The World Congress in Computer Science, Computer Engineering and Applied Computing (WorldComp), p. 228.
- Khatib, O., 1987. A unified approach for motion and force control of robot manipulators: The operational space formulation. *IEEE Journal on Robotics and Automation* **3(1)**, pp. 43–53.
- Kim, U., Lee, D. H., Kim, Y. B., Seok, D. Y., So, J., & Choi, H. R., 2017. S-surge: Novel portable surgical robot with multiaxis force-sensing capability for minimally invasive surgery. *IEEE/ASME Transactions on Mechatronics* **22(4)**, pp. 1717–1727.
- Konietschke, R., Hagn, U., Nickl, M., Jorg, S., Tobergte, A., Passig, G., Seibold, U., Le-Tien, L., Kubler, B., Groger, M. et al., 2009. The dlr mirosurge-a robotic system for surgery. In *Robotics and Automation, 2009. ICRA'09. IEEE International Conference on*. IEEE, pp. 1589–1590.
- Kosari, S. N., Ramadurai, S., Chizeck, H. J., & Hannaford, B., 2013. Control and tension estimation of a cable driven mechanism under different tensions. In *ASME 2013*

International Design Engineering Technical Conferences and Computers and Information in Engineering Conference. American Society of Mechanical Engineers, pp. V06AT07A077–V06AT07A077.

- Kuo, C.-H. & Dai, J. S., 2012. Kinematics of a fully-decoupled remote center-of-motion parallel manipulator for minimally invasive surgery. *Journal of Medical Devices* **6(2)**, p. 021008.
- Kwoh, Y. S., Hou, J., Jonckheere, E. A., & Hayati, S., 1988. A robot with improved absolute positioning accuracy for ct guided stereotactic brain surgery. *IEEE Transactions on Biomedical Engineering* **35(2)**, pp. 153–160.
- Lee-Kong, S. & Feingold, D. L., 2013. The history of minimally invasive surgery. In *Seminars in Colon and Rectal Surgery*, vol. 24. Elsevier, pp. 3–6.
- Lilly, K. W. & Orin, D. E., 1991. Alternate formulations for the manipulator inertia matrix. *The International Journal of Robotics Research* **10(1)**, pp. 64–74.
- Lum, M. J., Friedman, D. C., Sankaranarayanan, G., King, H., Fodero, K., Leuschke, R., Hannaford, B., Rosen, J., & Sinanan, M. N., 2009. The raven: Design and validation of a telesurgery system. *The International Journal of Robotics Research* **28(9)**, pp. 1183–1197.
- Mack, M. J., 2001. Minimally invasive and robotic surgery. *Jama* **285(5)**, pp. 568–572.
- Mayer, H., Nagy, I., & Knoll, A., 2004. Kinematics and modelling of a system for robotic surgery. In *On Advances in Robot Kinematics*. Springer, pp. 181–190.
- Memon, S., Heriot, A. G., Murphy, D. G., Bressel, M., & Lynch, A. C., 2012. Robotic versus laparoscopic proctectomy for rectal cancer: a meta-analysis. *Annals of surgical oncology* **19(7)**, pp. 2095–2101.
- Michelin, M., Dombre, E., & Poignet, P., 2004a. Geometrical control approaches for minimally invasive surgery. In *Perspective in Image-Guided Surgery*. World Scientific, pp. 152–159.
- Michelin, M., Poignet, P., & Dombre, E., 2004b. Dynamic task/posture decoupling for minimally invasive surgery motions: simulation results. In *Intelligent Robots and Systems, 2004.(IROS 2004). Proceedings. 2004 IEEE/RSJ International Conference on*, vol. 4. IEEE, pp. 3625–3630.
- Nethery, J. F. & Spong, M. W., 1994. Robotica: a mathematica package for robot analysis. *IEEE Robotics & Automation Magazine* **1(1)**, pp. 13–20.
- Nguan, C., Girvan, A., & Luke, P. P., 2008. Robotic surgery versus laparoscopy; a comparison between two robotic systems and laparoscopy. *Journal of robotic surgery* **1(4)**, pp. 263–268.

- Ortmaier, T. & Hirzinger, G., 2000. Cartesian control issues for minimally invasive robot surgery. In *Intelligent Robots and Systems, 2000.(IROS 2000). Proceedings. 2000 IEEE/RSJ International Conference on*, vol. 1. IEEE, pp. 565–571.
- Rao, P. P., 2018. Robotic surgery: new robots and finally some real competition! *World journal of urology* **36(4)**, pp. 537–541.
- Sandoval, J., Poisson, G., & Vieyres, P., 2017. A new kinematic formulation of the rcm constraint for redundant torque-controlled robots. In *2017 IEEE International Conference on Intelligent Robots and Systems (IROS)*.
- Schlenk, C., Bahls, T., Tarassenko, S., Klodmann, J., Bihler, M., & Wuesthoff, T., 2018. Robot integrated user interface for physical interaction with the dlr miro in versatile medical procedures. *Journal of Medical Robotics Research* **3(02)**, p. 1840006.
- Stringfield, S. B., Parry, L., Eisenstein, S., Horgan, S., Kane, C. J., & Ramamoorthy, S. L., 2017. Ten-year review of robotic surgery at an academic medical center. *Journal of the American College of Surgeons* **225(4)**, p. S79.
- Stürz, Y. R., Affolter, L. M., & Smith, R. S., 2017. Parameter identification of the kuka lbr iiwa robot including constraints on physical feasibility. *IFAC-PapersOnLine* **50(1)**, pp. 6863 – 6868. 20th IFAC World Congress.
- Vitiello, V., Lee, S.-L., Cundy, T. P., & Yang, G.-Z., 2013. Emerging robotic platforms for minimally invasive surgery. *IEEE reviews in biomedical engineering* **6**, pp. 111–126.
- Wagner, C. R., Stylopoulos, N., Jackson, P. G., & Howe, R. D., 2007. The benefit of force feedback in surgery: Examination of blunt dissection. *Presence: teleoperators and virtual environments* **16(3)**, pp. 252–262.
- Yilmaz, N., Bazman, M., & Tumerdem, U., 2018. External force/torque estimation on a dexterous parallel robotic surgical instrument wrist. In *International Conference on Intelligent Robots and Systems (IROS)*.
- Yu, C., Jin, M., & Liu, H., 2012. An analytical solution for inverse kinematic of 7-dof redundant manipulators with offset-wrist. In *Mechatronics and Automation (ICMA), 2012 International Conference on*. IEEE, pp. 92–97.



APPENDICES

Appendix A. 1 SENHANCE SYSTEM AND DA-VINCI COMPARISON TABLE

The comparison table between Senhance system and Da Vinci as quoted from the clearance report of the FDA (Food and Drug Administration, 2017).

Figure A.1: Senhance system and Da-Vinci comparison table

Feature	Senhance	Predicate
Surgeon Console	Open Cockpit design	Head-in cockpit
Surgeon Controls	Laparoscopic style grip and motion	Three-finger grip with open surgery motion
Instrument Activation	Dual surgeon inputs for manipulator arm motion (fingers in handles plus clutch pedal)	Dual surgeon inputs for manipulator arm motion (forehead sensor plus finger grip activation)
Endoscope Control	Hand or optional Infrared Eye sensor	Clutch pedal selection and hand control
Force Feedback	Yes	No
Surgeon Display	Active instruments shown	Similar
Robotic Arms	Three separate carts with one arm each	One cart with 3-4 arms
	Manual brake and wheels	Powered brake and wheels
	Exceeding Force Stop –arms stop when excessive force is detected	Arms stop after collision when joints are moved from original position
	Emergency Stop button	Similar
Surgical Instruments	Fulcrum set by force sensor	Fulcrum set by remote center function using potentiometers
	Straight stick standard laparoscopy	Wristed instruments
	Reusable instruments	Reusable instruments
Third Party Endoscope Adapters	Yes	No
Drapes	Third party sterile equipment covers	Same

Appendix A. 2 TUBITAK PROJECT WORK PACKAGES

TUBITAK Project No: 115E712 Work packages

Work package number	Work package name	Group
1	5 Degree of freedom forceps prototype mechanical design, analysis, production	Marmara University
1.1	Computer-aided mechanical design and analysis	Marmara University
1.2	Preparations for manufacturing, selection of materials and supply	Marmara University
1.3	Large pre-prototype manufacturing and assembly, testing	Marmara University
1.4	Manufacturing and assembly of final design, tests	Marmara University

Work package number	Work package name	Group
2	5-degree-of-freedom Forceps Prototype Control and Drive System Design, Analysis and Integration	Marmara University
2.1	Pre-study, control system requirements selection and supply of machinery / equipment	Marmara University
2.2	Kinematic and dynamic system modeling, computer modeling and simulations	Marmara University
2.3	Computer control algorithms developing	Marmara University
2.4	Establishment of the control system infrastructure (engines, computer, software, control box, etc.) and manufactured with large-scale pre-prototype mechanism integration	Marmara University
2.5	Motion and force control with 2.5 prototypes and double directional teleoperation experiments	Marmara University
2.6	Real-size prototype of the control system infrastructure creation and integration	Marmara University
2.7	Motion and force control with the final prototype and double directional teleoperation experiments, controller calibration	Marmara University
2.8	Laparoscopic surgery simulator with phantom palpation tests	Marmara University

Work package number	Work package name	Group
3	7 Degree of freedom Force Design, Analysis, integration	Marmara University Bahcesehir University
3.1	Kuka LBR robot restores the force of the robot feed remote motion control system design and application	Marmara University Bahcesehir University
3.2	Kinematic and dynamic system modeling, computer modeling and simulations	Marmara University Bahcesehir University
3.3	Kuka and 5 degree of freedom forceps system computer integration simulations	Marmara University Bahcesehir University
3.4	3.4 Motion on the laparoscopic surgical simulator and force control experiments	Marmara University Bahcesehir University

Work package number	Work package name	Group
4	Haptic Device System Integration	Marmara University Bahcesehir University
4.1	The design of the gripper integration and testing	Marmara University
4.2	Virtual reality of the haptic device testing, verification and optimization	Bahcesehir University
4.3	Haptic device software, robotic forceps software Integration	Bahcesehir University
4.4	Integrated robotic forceps system and haptic device, laparoscopic surgery simulator and experiments on phantoms and final tests	Marmara University Bahcesehir University

CURRICULUM VITAE

Name Surname : Alaa Alassi

Date and Place of Birth : 21/3/1989 Hasake

M.S.: Bahçeşehir University, Mechatronics Engineering

B.S. : Bahçeşehir University, Mechatronics Engineering

Publications :A. Alassi, N. Yilmaz, M. Bazman, B. Gur and U. Tumerdem, ”
Development and Kinematic Analysis of a Redundant, Modular and Backdrivable
Laparoscopic Surgery Robot,” 2018 IEEE/ASME International Conference on
Advanced Intelligent Mechatronics (AIM), Auckland, New Zealand, 2018.

Work Experience :

- Research Assistant, Bahcesehir University, Istanbul, Ongoing since June 2016.